Am J Physiol Cell Physiol 315: C164–C185, 2018.
First published March 21, 2018; doi:10.1152/ajpcell.00064.2017.

RESEARCH ARTICLE

Loss of *Parkin* impairs mitochondrial function and leads to muscle atrophy

Nesibe Peker,[1] Vinay Donipadi,[2] Mridula Sharma,[3] Craig McFarlane,[2]* and Ravi Kambadur[1]*

[1]*School of Biological Sciences, Nanyang Technological University, Singapore;* [2]*Cell and Molecular Biology Group, Singapore Institute for Clinical Sciences, Singapore; and* [3]*Department of Biochemistry, Yong Loo Lin School of Medicine, National University of Singapore, Singapore*

Submitted 20 March 2017; accepted in final form 18 March 2018

Peker N, Donipadi V, Sharma M, McFarlane C, Kambadur R. Loss of *Parkin* impairs mitochondrial function and leads to muscle atrophy. *Am J Physiol Cell Physiol* 315: C164–C185, 2018. First published March 21, 2018; doi:10.1152/ajpcell.00064.2017.—Parkinson's disease is a neurodegenerative disease characterized by tremors, muscle stiffness, and muscle weakness. Molecular genetic analysis has confirmed that mutations in *PARKIN* and *PINK1* genes, which play major roles in mitochondrial quality control and mitophagy, are frequently associated with Parkinson's disease. PARKIN is an E3 ubiquitin ligase that translocates to mitochondria during loss of mitochondrial membrane potential to increase mitophagy. Although muscle dysfunction is noted in Parkinson's disease, little is known about the involvement of *PARKIN* in the muscle phenotype of Parkinson's disease. In this study, we report that the mitochondrial uncoupler CCCP promotes PINK1/PARKIN-mediated mitophagy in myogenic C2C12 cells. As a result of this excess mitophagy, we show that CCCP treatment of myotubes leads to the development of myotube atrophy in vitro. Surprisingly, we also found that siRNA-mediated knockdown of *Parkin* results in impaired mitochondrial turnover. In addition, knockdown of *Parkin* led to myotubular atrophy in vitro. Consistent with these in vitro results, *Parkin* knockout muscles showed impaired mitochondrial function and smaller myofiber area, suggesting that *Parkin* function is required for post-natal skeletal muscle growth and development.

atrophy; mitochondria; mitochondrial turnover; Parkin; skeletal muscle

INTRODUCTION

Parkinson's disease (PD) is a progressive neurodegenerative disorder characterized by tremors, stiffness of skeletal muscle, slow motor activities (bradykinesia), depression, and dementia (70). The pathology of PD is defined as loss of dopaminergic neurons in substantia nigra pars compacta and subsequent formation of Lewy bodies, which consist primarily of α-synuclein inclusions (7). Previous studies have also documented that dopaminergic neurons in PD patients have abnormal mitochondrial activity, morphology, and mitochondria clearance (12, 48). Whereas the onset of the sporadic form of PD is thought to occur from 50 yr of age, patients with familial Parkinsonism develop symptoms as early as 20 yr of age, which is referred to as juvenile PD. Importantly, inherited PD accounts for up to 10% of all PD patients (18). Genetic studies have identified six genes linked to the autosomal recessive form of PD: *PARKIN* (*PARK2*), *PINK1* (*PARK6*), *DJ-1* (*PARK7*), *SCNA*, and *LRRK2*. Further investigation revealed that these genes are involved in regulation of mitochondrial turnover and mitochondrial biogenesis, suggesting that mitochondrial dynamics are altered in PD (76). Mutations in the *PARKIN* gene are the most common cause of familial PD and in fact, mutation of *PARKIN* is responsible for almost 80% of early onset PD (40). Studies have revealed that the E3 ligase PARKIN and PTEN-induced putative kinase 1 (PINK1) function together to regulate mitochondrial turnover and mitophagy, which is a selective form of autophagy that targets mitochondria (50). PINK1 activates PARKIN through phosphorylation of PARKIN at Ser65, which occurs when mitochondrial membrane potential is disrupted (62). Recently, three different groups have independently reported that in addition to PARKIN, PINK1 phosphorylates ubiquitin (29, 31, 52). According to these studies it was proposed that PINK1 phosphorylation of ubiquitin aids in recruitment of PARKIN to the outer mitochondrial membrane of mitochondria and further leads to hyperactivation of PARKIN. Subsequent recruitment of PARKIN to depolarized mitochondria leads to ubiquitin-mediated degradation of downstream targets including the mitochondrial fusion proteins mitofusin-1 (MFN1) and mitofusin-2 (MFN2) (20, 69). Degradation of mitofusin proteins and subsequent activation of mitochondrial fission prevents fusion of damaged mitochondria with healthy mitochondria (71). Dysfunctional mitochondria are then directed to autophagosome by the autophagy adaptors p62 and LC3 and degraded (17, 80). However, mutations in *PARK2* in PD result in accumulation of mitochondrial substrates of PARKIN, which leads to toxicity in dopaminergic neurons (19). In addition, *PARK2* mutations have been shown to lead to disrupted mitochondrial morphology and mitochondrial dysfunction in PD patients (23).

As mentioned above, skeletal muscles are also affected in patients with PD. Individuals with PD have impaired motor activity, which is associated with loss of skeletal muscle mass, muscle weakness, fatigue, and resistance to exercise (11, 14, 67). In addition, PD patients have atrophied pharyngeal muscle, which is associated with a switch from fast to slow fiber types (46). Although changes in muscle mass and function are noted in individuals with PD, the molecular mechanisms behind the skeletal muscle phenotype in PD are not well understood. Skeletal muscle is the largest tissue in the body and apart from supporting movement and mobility, skeletal muscle also maintains whole body energy metabolism by oxidizing glucose and fatty acids in mitochondria. Hence, maintaining healthy mitochondrial is vital for normal energy metabolism and preservation of skeletal muscle (59). Consistent with loss of muscle mass and muscle weakness, previous studies have demon-

* C. McFarlane and R. Kambadur are co-senior authors.
Address for reprint requests and other correspondence: R. Kambadur, Hamilton, New Zealand (e-mail: kambadur61@gmail.com).

 0363-6143/18 Copyright © 2018 the American Physiological Society

Downloaded from journals.physiology.org/journal/ajpcell (065.021.193.086) on February 24, 2022.

strated that PD patients also have impaired mitochondrial function in muscle tissue, with a reduction in mitochondrial complex activity noted (2, 5, 75).

Under conditions of muscle disuse and in response to chronic illness, skeletal muscle mass is lost, through a process known as skeletal muscle atrophy and/or wasting. Several studies have shown that skeletal muscle wasting and subsequent loss of myofibrillar proteins is mediated primarily through the action of the ubiquitin proteasome system and muscle-specific E3 ligases atrogin-1 and muscle RING finger protein 1 (MuRF1) (1, 26). In addition to ubiquitination of intracellular proteins, mitochondria dysfunction is also seen during muscle wasting conditions (59). Furthermore, loss of mitochondria due to mitophagy has also been shown to result in muscle wasting (54). Notably, studies have reported abnormalities in mitochondria during aging-related muscle wasting (sarcopenia) (4, 36), muscle wasting associated with chronic illness (cachexia) (28), and disuse atrophy (54).

In the fly model system, knockout of *parkin* results in abnormal wing posture and reduced climbing activity, suggesting that flight muscle function is affected (22). Also, a recent study has reported the presence of a hyperfused mitochondrial network and increased cell death in skeletal muscle of *Drosophila* lacking *parkin* (81). In addition, primary cultures isolated from newborn *Parkin* knockout (*Parkin* KO) mice have shown increased sensitivity to mitochondrial toxins and β-amyloid protein Aβ, which is restored by lentiviral-mediated overexpression of *Parkin*, suggesting that *Parkin* has a protective role in skeletal muscle (60). Another study has shown that loss of *Parkin* alleviates denervation-induced atrophy in soleus muscle of mice, which is presumably due to its involvement in autophagy-mediated denervation (13, 68). In addition to skeletal muscle atrophy, *Parkin* KO myotubes display impaired respiratory capacity and reduced insulin sensitivity (10). Furthermore, a recent study has revealed a role for PARKIN in regulating mitochondrial biogenesis by degrading Parkin-interacting substrate (PARIS), which normally functions to repress the expression of peroxisome proliferator-γ coactivator-1α (PGC-1α) (6, 63).

Since PD is associated with muscle weakness, muscle atrophy, and impaired mitochondrial function in skeletal muscle, we have utilized a model of mitophagy and performed *Parkin* loss of function studies to further define the role of *Parkin* in regulation of skeletal muscle mass and mitochondrial quality in skeletal muscle. Carbonyl cyanide m-chlorophenyl hydrazone (CCCP)-mediated activation of the PINK1/PARKIN pathway resulted in impaired mitochondrial function and myotubular atrophy in vitro. Also, loss of *Parkin* led to mitochondrial dysfunction, elevated levels of reactive oxygen species (ROS), and impaired mitochondrial turnover, while preserving mitochondrial mass. Moreover, loss of *Parkin* resulted in a muscle atrophy phenotype both in vitro and in vivo. Taken together, these data underscore the critical function of PARKIN in regulating mitochondrial function and muscle size in mice.

MATERIALS AND METHODS

Animals. Wild-type C57BL/6J mice were purchased from Biological Resource Centre, Singapore. *Parkin* knockout (*Parkin* KO) mice (*Park2*^{tm1Shn}) with C57BL/6J background were purchased from The Jackson Laboratory (Sacramento, CA). All mice used in this study were male. Mice were housed in a temperature (20–22°C) and light (12:12-h light-dark)-controlled facility (Nanyang Technological University Animal Research Facility, Singapore). All experiments using mice were ethically approved by the Institutional Animal Care and Use Committee (IACUC, Singapore) and were conducted following successful completion of the Responsible Care and Use of Laboratory Animal Course (RCULAC, Singapore).

Cell culture and transient transfection. C2C12 mouse myoblasts (79) were obtained from American Type Culture Collection (Manassas, VA) and were maintained in proliferation medium, consisting of high-glucose Dulbecco's modified Eagle's medium (DMEM; GE Healthcare, Piscataway, NJ), supplemented with 10% fetal bovine serum (FBS) and 1% penicillin-streptomycin (P/S; GIBCO, Carlsbad, CA) in a 37°C, 5% CO_2 incubator. To induce myogenic differentiation, myoblasts were seeded at a density of 25,000 cell/cm^2 in six-well plates and after an overnight attachment period the medium was replaced with differentiation medium (DMEM, supplemented with 2% horse serum and 1% P/S). For CCCP treatment studies, 72 h differentiated myotubes were treated with either 10 μM CCCP, or an equal volume of DMSO (Sigma-Aldrich, St. Louis, MO). For siRNA transfection studies, nontargeting (Control) (D-001206-13-05) and *Parkin*-specific (M-065413-01-0005) SMARTpool siRNA solutions were purchased from Dharmacon RNAi Technologies (Lafayette, CO). Sequences of siRNA present in the nontargeting siRNA pool were: 5′-UAG CGA CUA AAC ACA UCA A-3′, 5′-UAA GGC UAU GAA GAG AUA C-3′, 5′-AUG UAU UGG CCU GUA UUA G-3′, 5′-AUG AAC GUG AAU UGC UCA A-3′. Sequences of siRNA present in the murine *Parkin*-specific siRNA pool were: 5′-CGA AUC ACC UGA CGG UUC A-3′, 5′-ACA CGU CGG UAG CUU UGA A-3′, 5′-ACU CAA CGA UCG GCA GUU U-3′, 5′-GAG GAA UGC GUG CUG CAA A-3′. Myoblasts and 72 h differentiated myotubes were transfected with 25 nM of each siRNA solution using DharmaFECT 1 Transfection Reagent for 48 h as per the manufacturer's protocol (Thermo Fisher Scientific, Waltham, MA), after which cells were harvested for downstream analyses. To assess autophagic flux myoblasts were treated with 100 μM chloroquine, an autophagy inhibitor, for 6 h, before protein collection and subsequent immunoblotting analysis.

Primary myoblast isolation and tissue dissection. Wild-type and *Parkin* KO mice were euthanatized through CO_2 asphyxiation between 4 and 6 wk of age. Body weights, skeletal muscle weights, and tibia lengths were recorded for all mice. Primary myoblasts were isolated from hindlimb muscles using a preplating technique, as described in detail previously (43). Musculus (M) quadriceps (Quad), M. gastrocnemius (Gas), M. tibialis anterior (TA), M. soleus (Sol), and M. extensor digitorum longus (EDL) hindlimb muscles were dissected for subsequent biochemical and histological analysis. For hindlimb muscle weight analysis, average weights from left and right hindlimb muscles were normalized to average tibia lengths. Tissue samples were snap frozen in liquid nitrogen for biochemical analyses or embedded in OCT using liquid nitrogen-cooled isopentane (Sigma-Aldrich for myofiber cross-sectional analysis.

Protein extraction and Western blot analysis. To isolate total protein, cells were washed with ice-cold PBS and lysed in complete RIPA buffer [1% IGEPAL, 0.1% SDS, 0.5% (wt/vol) Na deoxycholate (wt/vol), 50 mM NaF, 0.2 mM Na_3VO_4, 1 mM PMSF, cOmplete Mini EDTA-free Protease Inhibitor, PhosSTOP (Sigma-Aldrich)] and were triturated 25 times using 26-gauge needles. To isolate protein from tissues, ~50 mg of skeletal muscle tissue was lysed using the Qiagen Tissue Lyser-II instrument (Qiagen, Valencia, CA) for 3× rounds of 30.0 Hz for 2 min each. Owing to ethical considerations relating to mouse numbers and required tissue amounts, gastrocnemius (Gas) muscle was selected, as opposed to the very small more oxidative soleus muscle, in this study, unless otherwise stated. Cells and tissue samples were then centrifuged at 10,000 *g* for 10 min at 4°C and the total cell/tissue protein containing supernatant was collected. Protein concentration was estimated using Bio-Rad (Bradford) protein assay reagent, according to the manufac-

Downloaded from journals.physiology.org/journal/ajpcell (065.021.193.086) on February 24, 2022.

turer's instructions (Bio-Rad, Hercules, CA). Proteins from mitochondrial fractions were isolated using the Mitochondria Isolation Kit for Cultured Cells (Thermo Fisher Scientific), Mitochondria Isolation Kit for Cells (Abcam, Cambridge, UK), or the Mitochondria Isolation Kit for Tissue (Abcam), as per respective manufacturer's instructions. For Western blot analysis, equal amounts of protein were resolved on 4–12% Bis-Tris precast gels. For LC3B/MAPLC3B immunoblotting, 30 μg of each protein samples was separated on either 4–12% Bis-Tris or 18% Tris-glycine precast gels (Invitrogen, Carlsbad, CA). Proteins were then transferred onto nitrocellulose membranes (Bio-Rad) using either the iBlot 2 dry blotting system or the XCell II Blot Module wet transfer system (Invitrogen). Wet transfer was performed at room temperature at constant voltage (30 V) for 2 h using transfer buffer [25 mM Tris Base, 190 mM glycine (Sigma-Aldrich) 20% methanol (Millipore, Billerica, MA)]. To detect antigen levels, membranes were blocked for 1 h at room temperature and hybridized with specific primary antibodies, overnight at 4°C. Details of primary antibodies, including company, catalog number, dilution, and blocking solution are provided in Table 1. Following overnight hybridization with primary antibodies, membranes were probed with species-specific horseradish peroxidase (HRP)-conjugated secondary antibodies for 1 h at room temperature. Secondary antibodies used were goat anti-rabbit HRP (catalog no. 1706515; Bio-Rad) or goat anti-mouse HRP (catalog no. 1706516; Bio-Rad). Immunoreactive bands were detected using Western Lightning Plus-ECL Enhanced Chemiluminescence Substrate (Perkin Elmer, Waltham, MA) and either autoradiography films or the ChemiDoc Touch Imaging System (Bio-Rad). To quantify intensity of immunoreactive bands, films were scanned using the GS-800 calibrated densitometer and analyzed using the Quantity One software package (Bio-Rad), whereas ChemiDoc Touch images were analyzed using Image Lab Software (Bio-Rad). Graphs represent mean intensity values following background subtraction.

RNA extraction and real-time quantitative PCR. RNA was isolated with TRIzol Reagent, according to the manufacturer's protocol (Thermo Fisher Scientific). One microgram RNA was reverse transcribed using the iScript cDNA Synthesis Kit and real-time quantitative PCR (qPCR) analysis was performed using the CFX96 Touch Real-Time PCR Detection System and SsoFast EvaGreen Supermix, as per the manufacturer's instructions (Bio-Rad). qPCR conditions were: 98°C for 3 min, 40 cycles of 98°C for 15 s, 55–60°C for 10 s, and 72°C for 20 s, followed by a melting curve from 65°C to 95°C at an increment of 0.5°C in 10 s. Sequences of all primers used in this study are provided in Table 2. The sequences of the nuclear- and mitochondrial-encoded genes used in this study have been published previously (15). Gene expression was analyzed using $\Delta\Delta C_t$ method and results are represented as fold change.

Assessment of mitochondrial respiratory capacity and exogenous fatty acid oxidation. Mitochondrial respiration and exogenous fatty acid utilization were assessed in vitro using the XF^{e}24 extracellular flux analyzer, and the XF Cell Mito Stress Test Kit, as per the manufacturer's instructions (Agilent Technologies, Santa Clara, CA). To assess exogenous fatty acid utilization, the XF Cell Mito Stress Test Kit was used together with the XF Fatty Acid Oxidation (FAO) Assay protocol, as provided by the manufacturer (Agilent Technologies). For all experiments, myoblasts were seeded at a density of 15,000 cells/well in XF^{e}24 cell culture plates. The assay cartridge was hydrated at 37°C, in a non-CO_2 incubator overnight before commencing analysis. Proliferation medium was replaced with either XF Assay Medium (for XF Cell Mito Stress Assay) or Substrate-limited Medium (for simultaneous measurement of exogenous FAO) 30 min and 6 h before the assay run, respectively, and plates were incubated at 37°C, in non-CO_2 incubator. For the XF FAO assay, 1 mM sodium palmitate was conjugated to 0.17 mM BSA, as previously described (73). Following this, the BSA-conjugated palmitate solution was added into each well (87.5 μl/well) of the XF^{e}24 microplates to a final concentration of 200 μM. Three measurements were recorded before and after sequential injection of 1 μM oligomycin, 0.5 μM FCCP, and 0.5 μM antimycin/rotenone (Agilent Technologies). Protein concentrations were estimated for each well using Bio-Rad Protein Assay reagent (Bio-Rad). Basal respiration was recorded at rate 3 before oligomycin injection. Maximal respiration was calculated as the maximum respiration noted during rate 7, 8, or 9. Proton leak was calculated at rate 6. Spare respiratory capacity and ATP-linked respiration were determined by subtracting basal respiration from maximal respiration and proton leak from basal respiration, respectively. Nonmitochondrial respiration (minimum respiration during rate 10, 11, or 12) was subtracted from all respiratory calculations.

MitoTracker Red CMXRos and Green FM staining. For MitoTracker Red CMXRos staining, myoblasts were seeded on eight-well glass chamber slides (Thermo Fisher Scientific) and stained with 200 nM MitoTracker CMXRos Red (Thermo Fisher Scientific) for 20 min in the dark in a 37°C 5% CO_2 incubator. Excessive dye was removed by 3× washes with proliferation medium. Cells were fixed with 2% formaldehyde for 15 min followed by 4% formaldehyde for 10 min. Slides were mounted with SlowFade Gold Antifade Mountant medium containing DAPI (Thermo Fisher Scientific). Myoblasts were visualized using the Olympus BX61 WI confocal microscope and analyzed using the Olympus FV1000 viewer (Olympus Imaging, Central Valley, PA). For MitoTracker Green FM analysis, myoblasts were stained with 150 nM MitoTracker Green FM (Thermo Fisher Scientific) for 20 min at 37°C, trypsinized, and collected in conical tubes. Cell pellets were then resuspended in PBS, and FACS analysis was performed to detect MitoTracker Green FM immediately using the FACSCanto II flow cytometry system (BD Biosciences, Franklin Lakes, NJ). A total of 10,000 events from three replicate wells per experimental group were detected using the FITC channel. Fluorescence intensity was averaged and is represented as mean fluorescence intensity (MFI).

Assessment of mitochondrial Complex I and Complex II activity. To assess mitochondrial complex activity, mitochondrial fractions were isolated using either the Mitochondria Isolation Kit for cells or the Mitochondria Isolation Kit for tissue, according to manufacturer's

Table 1. *Antibodies used in this study*

Antibody	Company	Catalog No.	Dilution	Blocking Solution
p-AMPKα (Thr172)	Cell Signaling	2535	1 to 1000	5% milk
AMPKα	Cell Signaling	2532	1 to 1000	5% milk
p-eIF2α (Ser51)	Cell Signaling	9721	1 to 500	5% BSA
CHOP	Cell Signaling	5554	1 to 200	5% BSA
DRP1	Cell Signaling	8570	1 to 1000	5% milk
PINK1	Abcam	ab23707	1 to 1000	5% milk
PARKIN	Abcam	ab15954	1 to 1000	5% milk
PARKIN (PRK8)	Abcam	ab77924	1 to 1000	5% milk
COX IV	Abcam	ab14744	1 to 500	1% PVP
OXPHOS AB Cocktail	Abcam	ab110413	1 to 1000	5% milk
MFN1	Abcam	ab57602	1 to 1000	5% milk
HSP60	Abcam	ab46798	1 to 10000	5% milk
p62	Abcam	ab91526	1 to 5000	5% milk
MFN2	Santa Cruz	sc-100506	1 to 1000	5% milk
PERK	Santa Cruz	sc-13073	1 to 1000	5% milk
LC3B/MAP1LC3B	Novus Bio.	NB100–2220	1 to 500	5% milk
FIS1	BioVision	3491R-100	1 to 1000	5% milk
MyHC	DSHB	MF20	1 to 10000	5% milk
MyLC	DSHB	T14	1 to 10000	5% milk
GAPDH	Santa Cruz	sc-32233	1 to 10000	5% milk
α-TUBULIN	Sigma	T9026	1 to 10000	5% milk

Antibody name, source, catalog no., dilution, and solution used for blocking each antibody are provided. p, phospho-specific antibodies; PVP, blocking solution containing 1% polyvinylpyrrolidone (PVP), 1% polyethylene glycol (PEG), and 0.3% bovine serum albumin (BSA). CHOP, C/EBP homologous protein; COX IV, cytochrome *c*-oxidase subunit 4; DRP1, dynamin-related protein 1; eIF2α, eukaryotic initiation factor 2 α-subunit; HSP60, heat shock protein 60; MFN1, mitofusin-1; MyHC, myosin heavy chain; MyLC, myosin light chain.

Downloaded from journals.physiology.org/journal/ajpcell (065.021.193.086) on February 24, 2022.

Table 2. *Gene symbols and sequences of all forward and reverse primers used in this study*

Gene Symbol	Forward Primer Sequence	Reverse Primer Sequence
Mfn1	ATTGGGGAGGTGCTGTCTC	TTCGGTCATAAGGTAGGCTTT
Mfn2	AGATGTCCCTGCTCTTTTCTC	TGTGTTCCTGTGGGTGTCTT
Opa1	GATGACACGCTCTCCAGTGAAG	CTCGGGGCTAACAGTACAACC
Drp1	CGGTTCCCTAAACTTCACGA	GCACCATTTCATTTGTCACG
Fis1	AAGTATGTGCGAGGGCTGTT	GGCAGAGAGCAGGTGAGG
Mff	TCACATTTGGTGAGTGGGGC	TTTTCCGGGACCCTCATTCG
Nd1	TGCACCTACCCTATCACTC	ATTGTTTGGGCTACGGCTC
Nd2	ATGAGTAGGCCTGGAATT	ATCAGAAGTGGAATGGGG
Nd4	ATAATTATAACTAGCTCAATCTGC	TCGTAGTTGGAGTTTGCTAG
Nd4L	CTCACCATAGCCTTCTCAC	CGTAATCTGTTCCGTACGTG
Nd6	TGTATGAGGTTGATGATGTTGG	CCGCAAACAAAGATCACCC
Cytb	CTTTGGGTCCCTTCTAGGAGTCTG	GCTGTGGCTATGACTGCGAACAG
Co1	GCTGAAGGAGAAGGAGAA	ATACACATAGCTCTTCTCCC
Atp6	CCACACACCAAAAGGACGAACATGA	CGGACTGCTAATGCCATTGGTTG
Ndufa9	CATTACTGCAGAGCCACT	ATCAGACGAAGGTGCATGAT
Ndufb6	ATAACTTTTTGCGGGACGGG	CAGGAAAATCTCTCATTGGTG
Ndufs3	AGGAACATGGCGGCGGCTGC	ATTTCAGCCACATACTCTCC
Sdha	CATACTGTTGCAGCAGCACAGG	CCACCAAATGCACGCTGATA
Uqcrc1	CCTACAGCACTCGAGAGCAC	AGGTGTGCCCTGGAATGCTG
Uqcrc2	TCCCTCAAAGTTGCCCC	GCAAGACGTAGTAAATGTGAG
Uqcrfs	GATGTCAAGGTGCCCGACTT	GATCTCGATCTTCGACATGG
Cox4	GAGCACATGGGAGTGTTGTG	CTGTCTTCCATTCATTGGTGC
Atp5	GGTCATCCTTTGTTGGTGC	GAGAATTCCACCATCCCTTC
Parkin	AAACCGGATGAGTGGTGAGT	AGCTACCGACGTGTCCTTGT
Pink1	GCTGATCGAGGAGAAGCAG	GATAATCCTCCAGACGGAAGC
mtDNA (*CoI*)	GCCCCAGATATAGCATTCCC	GTTCATCCTGTTCCTGCTCC
nuDNA (*18S*)	TAGAGGGACAAGTGGCGTTC	CGCTGAGCCAGTCAGTGT
Gapdh	GATGATGACCCGTTTGGCTCC	ACGCTCGTGGAAAGAAAAGA
Ppia	GCATACGGGTCCTGGCATCTTGTCC	GTGGCAAAGTGAGATTGTTGCC

instructions (Abcam). Mitochondrial Complex I and Complex II enzymatic activity was measured using the Complex I Enzyme Activity Microplate Assay Kit (Abcam) and the Complex II Enzyme Activity Microplate Assay Kit (Abcam), respectively, as per the manufacturer's instructions. Briefly, to assess mitochondrial Complex I activity, 50 μg of mitochondrial protein was loaded into microplates that were precoated with specific Complex-I antibodies and incubated at room temperature for 3 h for hybridization. Wells were washed twice with 300 μl/well wash buffer, and 200 μl assay solution was added to each well. Plates were read in a kinetic mode at 450 nm for 30 min at 20-s intervals using the Bio-Rad xMark Spectrophotometer (Bio-Rad). For assessment of mitochondrial Complex II activity, 25 μg of mitochondrial protein was loaded into wells that were precoated with an anti-Complex II monoclonal antibody and incubated at room temperature for 2 h. Wells were washed twice with 300 μl of 1× buffer provided by the manufacturer. Following this, 40 μl lipid mix was added to each well to maintain the stability of Complex II activity and the microplate was incubated at room temperature for 30 min. A total of 200 μl of activity solution, which included ubiquinone, succinate, 2,6-diclorophenolindophenol (DCPIP), and activity buffer provided by the company, was added into each well, and microplate was read at 600 nm in a kinetic mode, for 60 min at 20-s intervals, using the Bio-Rad xMark Spectrophotometer (Bio-Rad). The production of ubiquinol by the enzyme leads to the reduction of the dye DCPIP which in turn reduces its absorbance at OD600 nm. The rate of decrease in absorbance was monitored, and the rate between two time points for all of the samples where the decrease in absorbance is the most linear is represented as a bar graph.

Assessment of cellular ROS production. C2C12 cells were seeded onto 96-well clear bottom black-walled microplates, allowed to attach overnight, then transfected with siRNA. At 24 h posttransfection, myoblasts were stained with 10 μM H_2DCFDA for 30 min, as per the manufacturer's instructions (Thermo Fisher Scientific). The H_2DCFDA stain was then removed and cells were washed once with 200 μl PBS/well, before a final volume of 100 μl of PBS was added to each well. Fluorescent intensity (excitation/emission: 492–495 nm/517–527 nm), which is an indication of ROS levels, was measured in quadruplicate using the Tecan 2000 fluorescent plate reader and iControl software (Tecan Group, Männedorf, Switzerland).

Measurement of mitochondrial superoxide. To measure the levels of mitochondrial superoxide, C2C12 myoblasts were seeded onto six-well plates. After overnight attachment, cells were transfected with either nontargeting siRNA (Control) or *Parkin*-specific siRNA (*Parkin*-siRNA). The next day, media were replenished with 2 ml of media containing either 5 μM MitoSOX reagent or vehicle (DMSO) and incubated for 15 min in the dark in a 37°C/5% CO_2 incubator. After 3× washes with warm proliferation medium, cells were trypsinized and collected in conical tubes. Cell pellets were then resuspended in PBS, and MitoSOX fluorescence was detected using the FACSCanto II flow cytometry system (BD Biosciences). A total of 10,000 events were detected from three replicate wells per experimental group using the PE channel. MitoSOX fluorescent intensity was averaged and represented as MFI.

Genomic DNA isolation and mtDNA copy number analysis. To determine mtDNA copy number, genomic DNA was extracted using the QIAamp DNA Mini Kit, according to the manufacturer's instructions (Qiagen, Valencia, CA). To quantify mtDNA copy number, qPCR analysis was performed using 100 ng (5 ng/μl) DNA and SsoFast EvaGreen Supermix, as per the manufacturer's instructions (Bio-Rad). The qPCR conditions used were as follows: 95°C for 5 min, 45 cycles of 95°C for 10 s, 60°C for 20 s, 72°C for 20 s followed by melting curve. Primers for the mitochondrial gene *CoI* and the nuclear gene *18S* are indicated in Table 2 and published previously (77). Results were analyzed using the $\Delta\Delta C_t$ method and are represented as fold change relative to *18S* nuclear DNA control.

Histological analysis. For H&E staining of CCCP-treated myotubes, myoblasts were seeded at 20,000 cells/cm^2 on Thermanox coverslips (Nunc, Rochester, NY) and differentiated as described above. Prior to staining, differentiated myotubes were fixed in a solution of 70% ethanol:formaldehyde:acetic acid (20:2:1) for 30 s.

Downloaded from journals.physiology.org/journal/ajpcell (065.021.193.086) on February 24, 2022.

Hematoxylin and eosin (H&E) staining was performed as previously described (43). For H&E staining of transfected myotubes, cells were seeded, differentiated, transfected, and stained on two or four-well tissue culture slides (Ibidi, Martinsried, Germany) and images were captured immediately after the last ethanol wash was performed. To perform H&E staining of muscle sections, 10-μm transverse sections were cut from the midbelly region of OCT-embedded TA muscles using the Leica CM1950 Cryostat (Leica Microsystems, Wetzlar, Germany). Hematoxylin and eosin staining of tissue sections was performed, as described previously (43). All H&E-stained samples were imaged using the Leica DM6000 B microscope (Leica Microsystems) and ×5 and ×10 objectives for muscle sections and myotubes, respectively. Myotube and myofiber areas were determined using ImageJ software (NIH, Bethesda, MD). For TA muscle sections, the area of 1,000 myofibers was calculated from each muscle section per genotype. For CCCP treatment, the area of 10 myotubes per image (n = 5, per coverslip) across 2–3 biological replicates per treatment group was calculated. For *Parkin* knockdown experiments, the area of 200 myotubes was measured across four biological replicates each for Control-siRNA and *Parkin*-siRNA-transfected myotubes. Results are

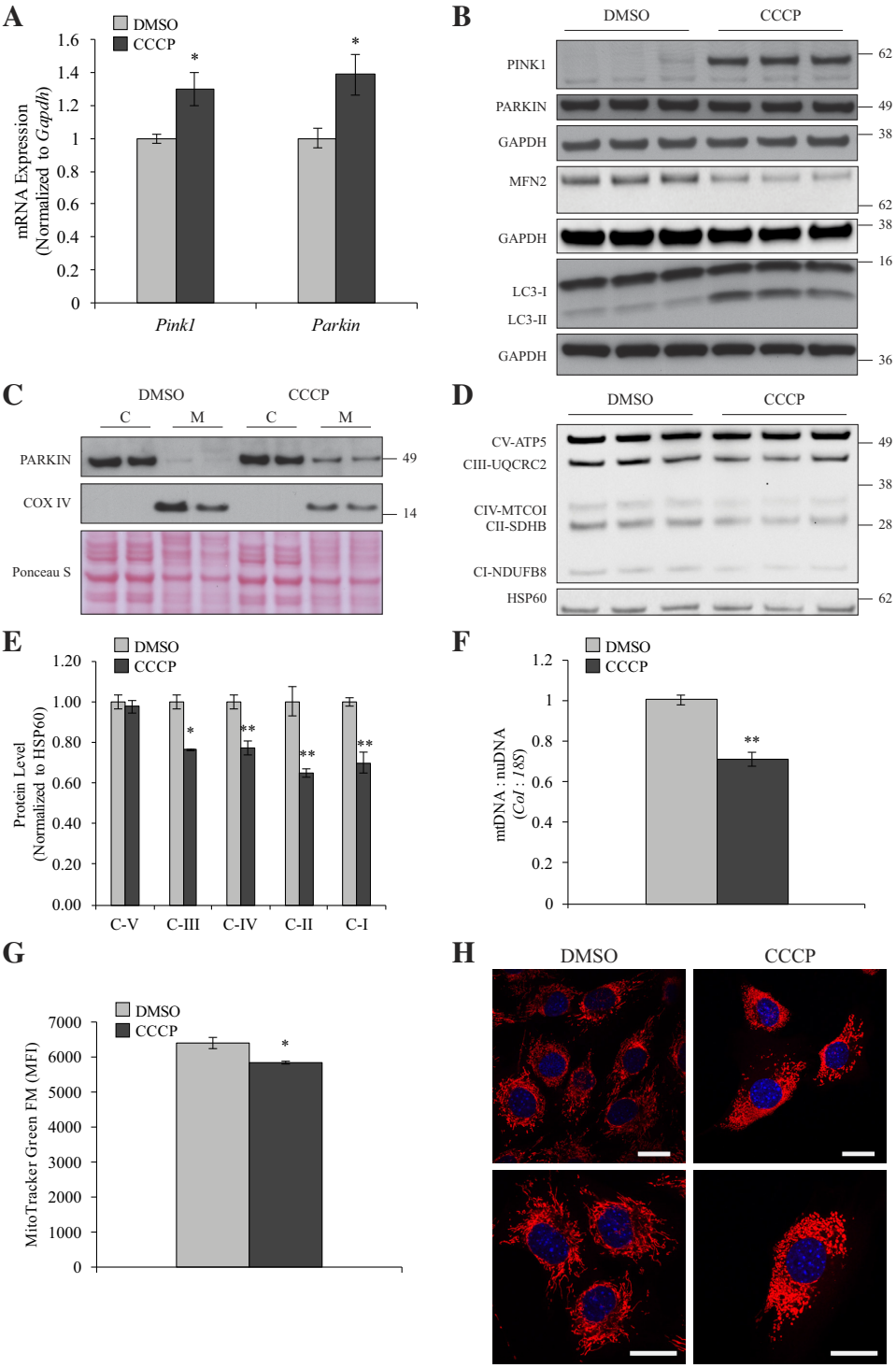

Fig. 1. CCCP induces PINK1/PARKIN-mediated mitophagy in C2C12 myotubes. *A*: graph showing real-time quantitative PCR (qPCR) analysis of *Pink1* and *Parkin* mRNA expression, normalized to *Gapdh*, in 24 h DMSO or 10 μM CCCP treated myotubes (n = 3). *B*: representative images of Western blot analysis of PINK1, PARKIN, mitofusin-2 (MFN2), nonlipidated LC3 (LC3-I), and lipidated LC3 (LC3-II) protein levels in DMSO and 10 μM CCCP-treated myotubes. The levels of GAPDH were assessed as a loading control (n = 3). *C*: representative images of Western blot analysis of PARKIN and cytochrome *c*-oxidase (COX) IV protein levels in cytosolic (C) and mitochondrial (M) fractions isolated from myotubes treated with either DMSO or 10 μM CCCP for 24 h. Ponceau S staining was performed as a loading control (n = 8). *D*: representative images of Western blot analysis of OXPHOS subunit (ATP5, UQCRC2, MTCOI, SDHB, and NDUFB8) protein levels in C2C12 myotubes treated with either DMSO or 10 μM CCCP for 24 h. The levels of heat shock protein 60 (HSP60) were assessed as a loading control (n = 3). *E*: graph showing quantification of OXPHOS protein levels, normalized to HSP60, in arbitrary units (n = 3). *F*: graph showing qPCR analysis of mitochondrial DNA (mtDNA) copy number:nuclear DNA (nuDNA) copy number ratio in myotubes treated with either DMSO or 10 μM CCCP for 24 h. Values are expressed as fold change relative to DMSO control. Expression of the mitochondrial gene *CoI* was normalized to the nuclear gene *18S* (n = 3). *G*: graph showing results of FACS analysis of MitoTracker Green FM-stained myoblasts following 24 h treatment with either DMSO or 10 μM CCCP (MFI, mean fluorescence intensity) (n = 3). *H*: representative confocal images of MitoTracker Red CMXRos-stained myoblasts treated with either DMSO or 10 μM CCCP for 24 h. DAPI (blue) was used to stain nuclei. *Top*: images reflect cells captured using the ×100 objective. *Bottom*: images are magnified further ×1.5 and captured using the Olympus BX61 WI confocal microscope. Scale bars, 20 μm. All graphs display means ± SE. $*P < 0.05$, $**P < 0.01$ (Student's *t*-test).

Downloaded from journals.physiology.org/journal/ajpcell (065.021.193.086) on February 24, 2022.

represented as a frequency-distribution graph. Average myotube area was also calculated.

Statistical analysis. F-tests were performed on each data set to test for equal variance between groups. Two-tailed Student's *t*-tests were conducted for statistical analysis to assess for differences between two groups, where the calculated F-value from the data sets is less than the F-critical value. Two-way ANOVA was applied for analysis of data from more than two groups, followed by Tukey's post hoc test. $P <$

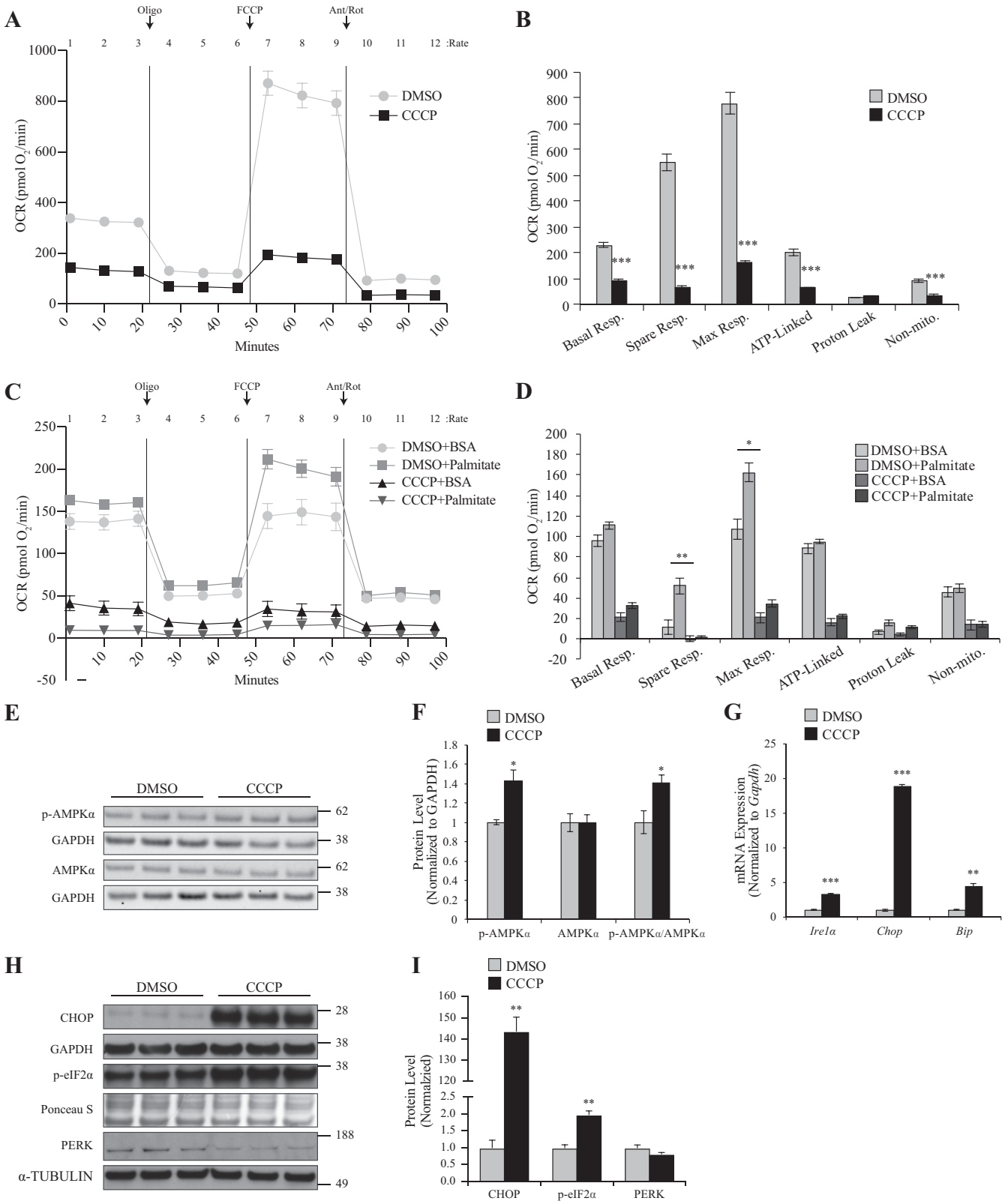

Downloaded from journals.physiology.org/journal/ajpcell (065.021.193.086) on February 24, 2022.

0.05 was considered statistically significant. Data are represented as means ± SE. Researchers were not blinded during the experiment plan and analysis. Details of biological replicates for each experiment are indicated in respective figure legends.

RESULTS

Treatment with CCCP promotes mitophagy and impaired mitochondrial function in C2C12 myotube cultures. To investigate if induction of mitophagy leads to atrophy of muscle cells, we first established a model of Parkin-mediated mitophagy by treating C2C12 myotubes with CCCP. Quantitative real-time PCR (qPCR) analysis revealed increased mRNA expression of both *Pink1* and *Parkin* following CCCP treatment (Fig. 1*A*). Subsequent immunoblot analysis revealed increased levels of full-length PINK1 following 24 h CCCP treatment in myotubes (Fig. 1*B*). However, no observable difference in PARKIN levels was noted upon CCCP treatment (Fig. 1*B*). Reduced levels of the mitochondrial fusion protein mitofusin 2 (MFN2) and enhanced levels of the autophagosomal marker LC3-II (lipidated LC3) were also observed in response to CCCP treatment of C2C12 myotube cultures (Fig. 1*B*). Despite no change in total PARKIN protein levels (Fig. 1*B*), treatment with CCCP resulted in increased levels of PARKIN protein in isolated mitochondrial fractions (Fig. 1*C*), which is consistent with both increased translocation of PARKIN to mitochondria and enhanced activation of PARKIN. Immunoblotting of critical mitochondrial OXPHOS proteins revealed that CCCP treatment results in a significant reduction in the levels of mitochondrial complex proteins necessary for oxidative phosphorylation (Fig. 1, *D* and *E*), with significantly lower levels of UQCRC2 (Complex III), MTCOI (Complex IV), SDHB (Complex II), and NDUFB8 (Complex I) noted upon CCCP treatment (Fig. 1, *D* and *E*). However, no significant difference in the Complex V protein ATP5 was observed following CCCP treatment (Fig. 1, *D* and *E*).

Next, we quantified mitochondrial DNA copy number and mitochondrial content through qPCR analysis and MitoTracker Green FM analysis, respectively. Results revealed a significant decrease in mtDNA copy number and MitoTracker Green FM intensity in myoblasts upon CCCP treatment (Fig. 1, *F* and *G*), which is indicative of decreased mitochondrial number. To visualize changes in mitochondrial architecture in response to CCCP treatment, we performed MitoTracker Red CMXRos staining and confocal microscopy (Fig. 1*H*). Subsequent assessment of mitochondria morphology revealed disruption of the typical filamentous mitochondria network, resulting in a punctate mitochondria morphology, which is consistent with mitochondria swelling and fragmentation, in response to CCCP treatment (Fig. 1*H*).

To investigate the effect of CCCP treatment on mitochondrial function, we next assessed oxygen consumption rate (OCR) using the Seahorse XF^{e}24 extracellular flux analyzer. A dramatic reduction in real-time oxygen consumption rate was noted in myotubes treated with CCCP, when compared with vehicle (DMSO)-treated controls (Fig. 2*A*). Indices of mitochondrial function were calculated, and a significant reduction in basal, maximal, ATP-linked, and nonmitochondrial respiration was noted upon treatment with CCCP (Fig. 2*B*). In addition, a significant reduction in spare respiratory capacity was further observed in CCCP-treated myotubes, when compared with vehicle controls (Fig. 2*B*). Given that mitochondria are the major site for fatty acid oxidation, we next measured real-time utilization of exogenous fatty acids (palmitate) using the Seahorse XF^{e}24 analyzer. Real-time OCR measurements revealed a dramatic reduction in OCR in myotubes treated with CCCP, in the presence of either BSA or palmitate (Fig. 2, *C* and *D*). Moreover, spare and maximal respiration, due to utilization of palmitate, was also significantly reduced in CCCP-treated myotubes (Fig. 2*D*).

AMPK is key energy sensor and regulator in cells; in fact, AMPK is activated in response to reduced levels of ATP and functions to switch off anabolic (energy utilizing) processes in favor of catabolic (energy producing) processes (25, 64). Therefore, we next sought to determine whether AMPK is activated in response to CCCP treatment. Consistent with reduced mitochondrial respiratory capacity, Western blot analysis revealed that CCCP treatment increased the levels of active phosphorylated AMPKα in C2C12 myotubes (Fig. 2, *E* and *F*).

Mitochondria and endoplasmic reticulum (ER) directly communicate through mitochondria-associated membranes. Owing to physical and functional connection, excessive ROS production, unfolded protein response (UPR), or failure to buffer calcium between two organelles might trigger a stress response in either or both organelles. In fact, shift of Ca^{2+} from ER lumen to mitochondria following mitochondrial dysfunction leads to flaws in protein folding machinery, thereby resulting in the accumulation of misfolded proteins (35). Therefore, we

Fig. 2. CCCP treatment results in mitochondrial dysfunction and endoplasmic reticulum (ER) stress in C2C12 myotubes. *A*: graph showing the real-time oxygen consumption rate (OCR) of myotubes treated with either DMSO or 10 μM CCCP for 24 h, as assessed by the Seahorse XF^{e}24 extracellular flux analyzer (n = 10). Time points where oligomycin (Oligo), FCCP and antimycin/rotenone (Ant/Rot) were injected and the rate number where each OCR was measured are indicated. *B*: graph showing quantification of basal, spare, maximal, ATP-linked, proton leak, and nonmitochondrial respiratory capacity in myotubes treated with either DMSO or 10 μM CCCP for 24 h (n = 10). *C*: graph showing the real-time assessment of exogenous fatty acid (palmitate) utilization in myotubes treated with either DMSO or 10 μM CCCP in the absence (BSA) or presence of palmitate for 24 h (n = 5). Time points where oligomycin (Oligo), FCCP, and antimycin/rotenone (Ant/Rot) were injected and the rate number where each OCR was measured are indicated. *D*: graph showing quantification of basal, spare, maximal, ATP-linked and nonmitochondrial respiration, and respiration due to proton leak in myotubes treated with either DMSO or 10 μM CCCP in the absence (BSA) or presence of palmitate for 24 h (n = 5). *E*: representative images of Western blot analysis of phosphorylated (p-AMPKα) and total AMPKα protein levels in myotubes treated with either DMSO or 10 μM CCCP for 24 h. The levels of GAPDH were assessed as a loading control (n = 3). *F*: graph showing quantification of p-AMPKα, total AMPKα, and the ratio of p-AMPKα/total AMPKα, normalized to GAPDH, in arbitrary units (n = 3). *G*: graph showing qPCR analysis of *Ire1α*, *Chop*, and *Bip* ER-stress marker mRNA expression, normalized to *Gapdh*, in 24 h DMSO or 10 μM CCCP-treated myotubes (n = 3). *H*: representative images of Western blot analysis of ER-stress marker [C/EBP homologous protein (CHOP), p-α-subunit of eukaryotic initiation factor 2 (eIF2α), and protein kinase RNA-like endoplasmic reticulum kinase (PERK)] protein levels in myotubes treated with either DMSO or 10 μM CCCP for 24 h. The levels of GAPDH, α-TUBULIN, or Ponceau S were assessed as loading controls (n = 3). *I*: graph showing quantification of CHOP, p-eIF2α, and PERK and normalized to GAPDH, Ponceau S, or α-TUBULIN, respectively, in arbitrary units (n = 3). All graphs represent means ± SE. *$P < 0.05$, **$P < 0.01$, ***$P < 0.001$ (Student's *t*-test) (significance in *D* was determined by using two-way ANOVA).

Downloaded from journals.physiology.org/journal/ajpcell (065.021.193.086) on February 24, 2022.

sought to determine whether CCCP-mediated mitophagy in C2C12 myotubes is associated with increased ER stress. Examination of ER stress indicators via qPCR analysis revealed upregulation of inositol requiring enzyme 1 (*Ire1α*), C/EBP homologous protein (*Chop*), and binding immunoglobulin protein (*BiP*) following CCCP treatment, suggesting that CCCP induces ER stress by upregulating UPR genes (Fig. 2*G*). Activation of ER stress results in dimerization of PERK, a

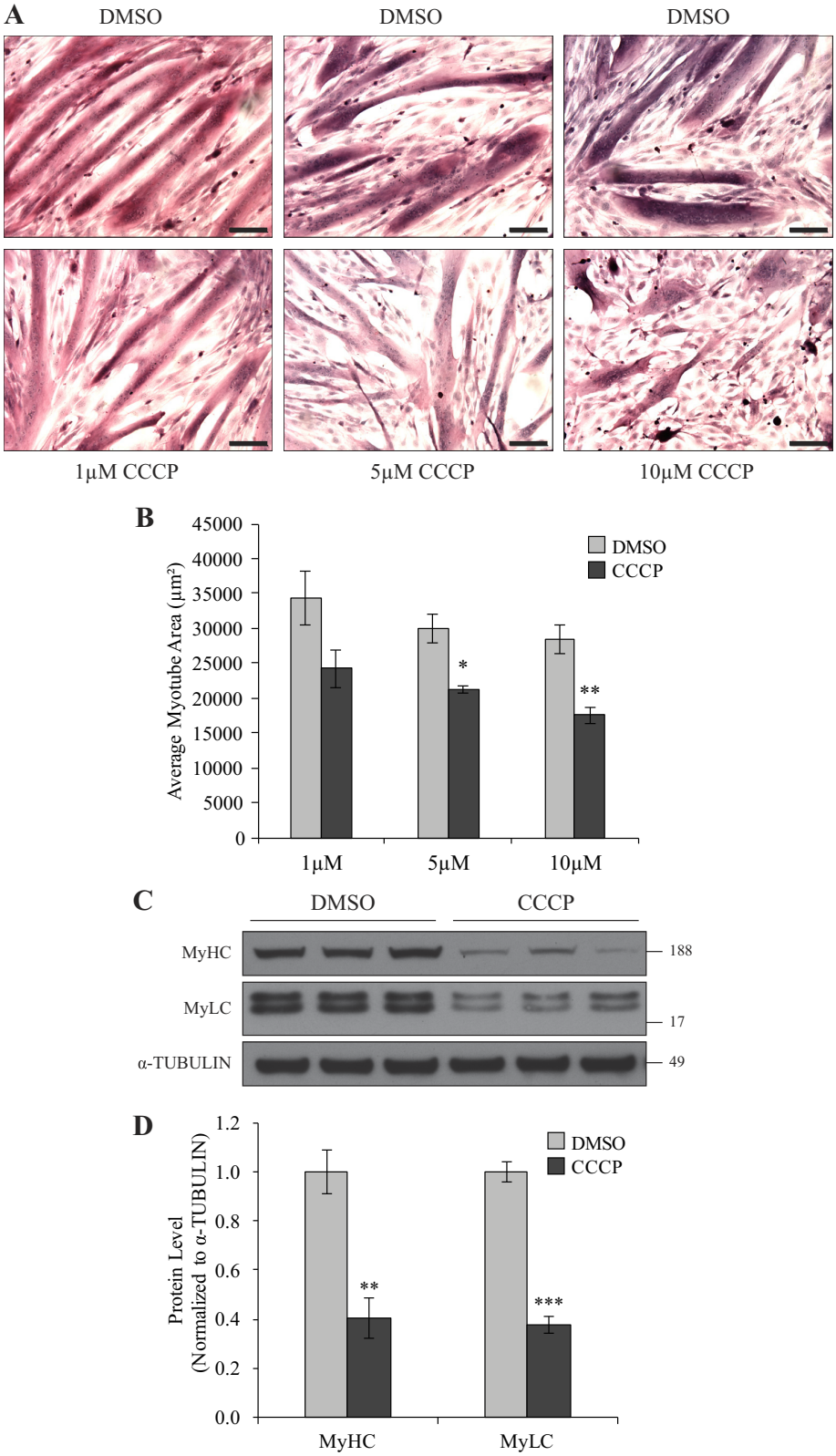

Fig. 3. CCCP treatment leads to myotube atrophy in vitro. *A*: representative images of hematoxylin and eosin (H&E)-stained 72 h differentiated C2C12 myotubes treated with either DMSO or increasing concentrations (1, 5, or 10 μM) of CCCP for 24 h. Scale bar, 100 μm. *B*: graph showing quantification of average myotube area in 72 h differentiated C2C12 myotubes treated with either DMSO or increasing concentrations of CCCP for 24 h (n = 2–3). *C*: representative images of Western blot analysis of myosin heavy chain (MyHC) and myosin light chain (MyLC) protein levels in myotubes treated with either DMSO or 10 μM CCCP for 24 h. The levels of α-TUBULIN were assessed as a loading control. *D*: graph showing quantification of MyHC and MyLC protein levels, normalized to α-TUBULIN, in arbitrary units (n = 3). All graphs display means ± SE. $^{*}P < 0.05$, $^{**}P < 0.01$, $^{***}P < 0.001$ (Student's t-test).

Downloaded from journals.physiology.org/journal/ajpcell (065.021.193.086) on February 24, 2022.

serine/threonine kinase, which phosphorylates and activates the α-subunit of eukaryotic initiation factor eIF2α, which in turn inhibits protein synthesis and activates the ER stress-mediated apoptosis pathway through CHOP. Consistent with this, an increase in the levels of total CHOP and phosphorylated eIF2α protein were observed following CCCP treatment, but the levels of PERK remained unchanged (Fig. 2, *H* and *I*), suggesting that CCCP-induced mitophagy activates the ER

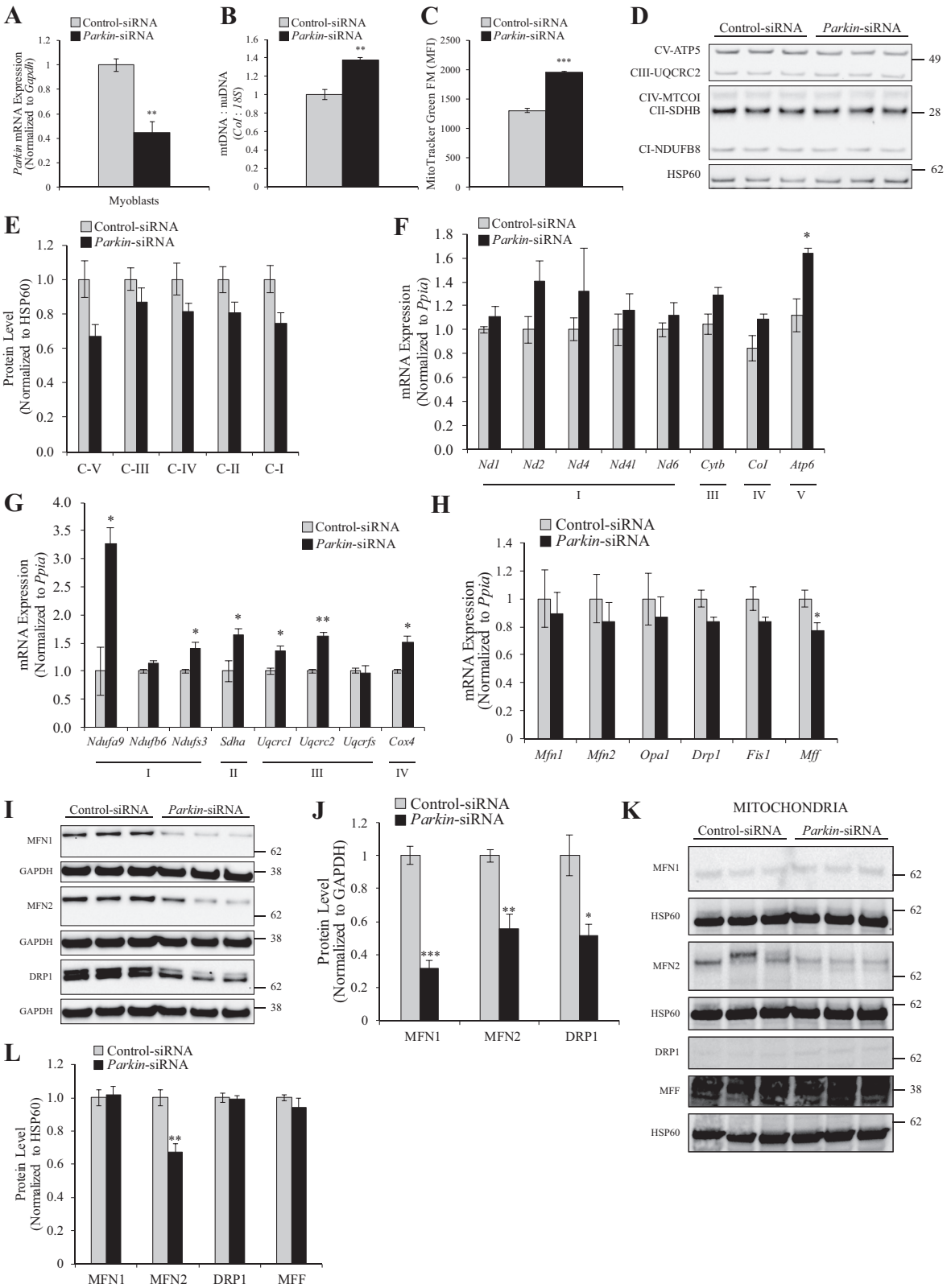

Downloaded from journals.physiology.org/journal/ajpcell (065.021.193.086) on February 24, 2022.

stress response in C2C12 myotubes. Taken together, these data suggest that CCCP treatment leads to activation of PARKIN, loss of mitochondria (mitophagy), impaired mitochondrial function, and ER stress in C2C12 myotubes.

Treatment of myotube cultures with CCCP leads to myotubular atrophy. To explore whether CCCP-induced loss of mitochondrial number and function resulted in skeletal muscle atrophy, differentiated C2C12 myotubes were treated with 1, 5, or 10 μM CCCP. Treatment with 5 and 10 μM CCCP led to an observable reduction in myotube area (Fig. 3*A*). Subsequent quantification of myotube area revealed a significant reduction in myotube area upon treatment with 5 and 10 μM CCCP (Fig. 3*B*). Consistent with this, myosin heavy chain and myosin light chain protein levels were significantly decreased upon CCCP treatment (Fig. 3, *C* and *D*). Collectively, these data reveal that treatment with CCCP results in a muscle atrophy phenotype in C2C12 myotubes.

Knockdown of Parkin results in accumulation of dysfunctional mitochondria in myoblast cultures. Next, we assessed the effect of *Parkin* knockdown on mitochondrial number and function in myoblasts. qPCR analysis revealed significant knockdown of *Parkin* in C2C12 myoblasts transfected with *Parkin*-specific siRNA (Fig. 4*A*). In contrast to the results observed following CCCP treatment, knockdown of *Parkin* in myoblasts resulted in a significant increase in mtDNA copy number (Fig. 4*B*) and MitoTracker Green FM intensity (Fig. 4*C*), consistent with an increase in mitochondrial content. Despite the increase in mitochondrial content noted in response to *Parkin* knockdown, the levels of critical OXPHOS proteins were not significantly altered between control and *Parkin* knockdown myoblasts (Fig. 4, *D* and *E*), and in fact, the levels of OXPHOS proteins tended to decrease upon *Parkin* knockdown (Fig. 4, *D* and *E*). In contrast, qPCR analysis revealed a significant increase in the expression of several mitochondrial complex genes in response to *Parkin* knockdown, with increased expression of *Atp6*, *Ndufa9*, *Ndufs3*, *Sdha*, *Uqcrc1*, *Uqcrc2*, and *Cox4* noted (Fig. 4, *F* and *G*). Interestingly, with the exception of *Atp6*, only nuclear DNA-encoded mitochondrial genes were upregulated (*Ndufa9*, *Ndufs3*, *Sdha*, *Uqcrc1*, *Uqcrc2*, and *Cox4*) upon *Parkin* knockdown in myoblasts (Fig. 4, *F* and *G*).

The increase in mitochondrial DNA copy number and mitochondrial content observed in *Parkin* knockdown myoblasts directed us to further analyze mitochondrial turnover. Reduced expression of mitochondrial fusion markers, mitofusin-1 (*Mfn1*), mitofusin-2 (*Mfn2*) and mitochondrial dynamin-like GTPase 1 (*Opa1*), and mitochondrial fission markers, dynamin-related protein 1 (*Drp1*), mitochondrial fission 1 protein (*Fis1*) and mitochondrial fission factor (*Mff*), was observed in *Parkin* knockdown myoblasts, although only the expression of mitochondrial fission factor (*Mff*) was significantly reduced (Fig. 4*H*). Moreover, the levels of MFN1, MFN2, and DRP1 proteins were significantly reduced in *Parkin* knockdown myoblasts (Fig. 4, *I* and *J*). Next, we assessed levels of mitochondrial turnover proteins in mitochondrial fractions isolated from myotubes transfected with either nontargeting (Control) siRNA or *Parkin*-specific siRNA. Western blot analysis revealed no significant difference in protein levels of mitochondrial turnover proteins, with the exception of MFN2, which was significantly reduced in response to *Parkin* knockdown (Fig. 4, *K* and *L*). These data suggest that knockdown of *Parkin* results in impaired mitochondrial turnover in vitro.

Increased mitochondrial content, together with reduced levels of mitochondrial fission and fusion markers, is suggestive of impaired mitochondrial turnover (65). Therefore, we next investigated whether knockdown of *Parkin* leads to excess autophagy through assessment of the levels of the autophagosomal markers LC3-II and p62. As shown in Fig. 5*A*, knockdown of *Parkin* reduced p62 protein levels, whereas no significant difference in endogenous LC3-I and LC3-II levels was noted between control and *Parkin* knockdown myoblasts (Fig. 5, *A* and *B*). Moreover, no notable difference in LC3-I and LC3-II levels was observed between control and *Parkin*-siRNA-transfected myoblasts in response to chloroquine treatment, suggesting that autophagic flux was not significantly altered in *Parkin* knockdown myoblasts (Fig. 5, *C* and *D*). Importantly, Western blot analysis did not reveal a significant difference in LC3-I and LC3-II protein levels in mitochondrial fractions collected from *Parkin* knockdown myotubes as compared with control (Fig. 5, *E* and *F*), further suggesting that loss of *Parkin* does not result in excess mitophagy. Taken together, these data suggest that the knockdown of *Parkin* in myoblasts results in accumulation of mitochondria, possibly because of impaired mitochondrial turnover.

Next, we assessed mitochondrial function using the Seahorse XF^{e}24 extracellular flux analyzer. A reduction in OCR

Fig. 4. *Parkin* knockdown leads to accumulation of dysfunctional mitochondria and impaired mitochondrial turnover in vitro. *A*: graph showing qPCR analysis of *Parkin* mRNA expression, normalized to *Gapdh*, in nontargeting siRNA (Control-siRNA) and *Parkin*-specific siRNA (*Parkin*-siRNA)-transfected myoblasts ($n = 3$). *B*: graph showing qPCR analysis of mtDNA copy number:nuDNA copy number ratio in Control-siRNA and *Parkin*-siRNA-transfected myoblasts. The expression of the mitochondrial gene *CoI* was normalized to the nuclear gene *18S* ($n = 3$). *C*: graph showing results of FACS analysis of MitoTracker Green FM-stained Control-siRNA and *Parkin*-siRNA-transfected myoblasts ($n = 3$). MFI, mean fluorescence intensity. *D*: representative images of Western blot analysis of OXPHOS subunit (ATP5, UQCRC2, MTCOI, SDHB, and NDUFB8) protein levels in Control-siRNA and *Parkin*-siRNA-transfected myoblasts. The levels of heat shock protein 60 (HSP60) were assessed as a loading control. Western blot was hybridized using mixture of five different antibodies on the same membrane. Two different exposures (two different boxes) of the same membrane are used to show the results ($n = 3$). *E*: graph showing quantification of OXPHOS protein levels, normalized to HSP60, in arbitrary units ($n = 3$). *F*: graph showing qPCR analysis of mitochondria DNA-encoded mitochondrial complex gene expression, normalized to *Ppia*, in Control-siRNA and *Parkin*-siRNA-transfected myoblasts ($n = 3$). *G*: graph showing qPCR analysis of nuclear DNA-encoded mitochondrial complex gene expression, normalized to *Ppia*, in Control-siRNA and *Parkin*-siRNA-transfected myoblasts ($n = 3$). *H*: graph showing qPCR analysis of mitochondrial fusion (*Mfn1*, *Mfn2*, *and Opa1*) and fission (*Drp1*, *Fis1*, and *Mff*) marker gene expression, normalized to *Ppia*, in Control-siRNA and *Parkin*-siRNA-transfected myoblasts ($n = 3$). *I*: representative images of Western blot analysis of mitofusin-1 (MFN1), MFN2, and dynamin-related protein 1 (DRP1) protein levels in Control-siRNA and *Parkin*-siRNA transfected myoblasts. The levels of GAPDH were assessed as a loading control for each respective blot ($n = 3$). J: graph showing quantification of MFN1, MFN2, and DRP1 protein levels, normalized to GAPDH, in arbitrary units ($n = 3$). *K*: representative images of Western blot analysis of MFN1, MFN2, DRP1, and mitochondrial fission factor (MFF) protein levels in mitochondrial fraction collected from Control-siRNA and *Parkin*-siRNA-transfected myotubes. The levels of HSP60 were assessed as a loading control for each respective blot ($n = 3$). *L*: graph representing quantification of MFN1, MFN2, DRP1, and MFF protein levels, normalized to HSP60, in arbitrary units ($n = 3$). All graphs display means ± SE. $^*P < 0.05$, $^{**}P < 0.01$, $^{***}P < 0.001$ (Student's *t*-test).

Downloaded from journals.physiology.org/journal/ajpcell (065.021.193.086) on February 24, 2022.

was noted in *Parkin* knockdown myoblasts, when compared with control (Fig. 6*A*). A significant reduction in basal and ATP-linked respiration was noted in *Parkin* knockdown myoblasts, together with a significant reduction in OCR due to proton leak (Fig. 6*B*). Although not statistically significant, a reduction in maximum respiration and spare respiratory capacity was further noted in *Parkin* knockdown myoblasts, when compared with controls (Fig. 6*B*). Next, we directly measured mitochondrial respiration in permeabilized myoblasts and, consistent with reduced mitochondrial respiration in intact cells, we noted a significant reduction in state 3 and state 4 respiration in *Parkin* knockdown cells (Fig. 6, *C* and *D*). We did not observe any significant change in respiratory control ratio (Fig. 6*D*). These data reveal that knockdown of *Parkin* results in reduced basal and ATP-linked respiration, as well as reduced state 3 and state 4 respiration in myoblasts. To investigate whether or not the reduced mitochondrial respiration resulted from impaired mitochondrial complex activity, we further assessed the activity of mitochondrial Complex I and Complex II in control and *Parkin*-siRNA transfected myoblasts. A decrease in mitochondrial Complex I enzymatic activity was noted over time in *Parkin*-siRNA-transfected myoblasts, when compared with controls (Fig. 6*E*), with a significant reduction noted at 24 and 28 min (Fig. 6*E*). We further noted an ~30% decrease in mitochondrial Complex II activity in *Parkin*-siRNA-transfected myoblasts, although the decrease was not statistically significant (Fig. 6*F*).

As mitochondria play an important role in detoxifying ROS in the cell, we next measured cellular ROS production to further assess mitochondrial function. Consistent with impaired mitochondrial function, we noted a moderate but significant increase in the levels of cellular ROS in *Parkin*

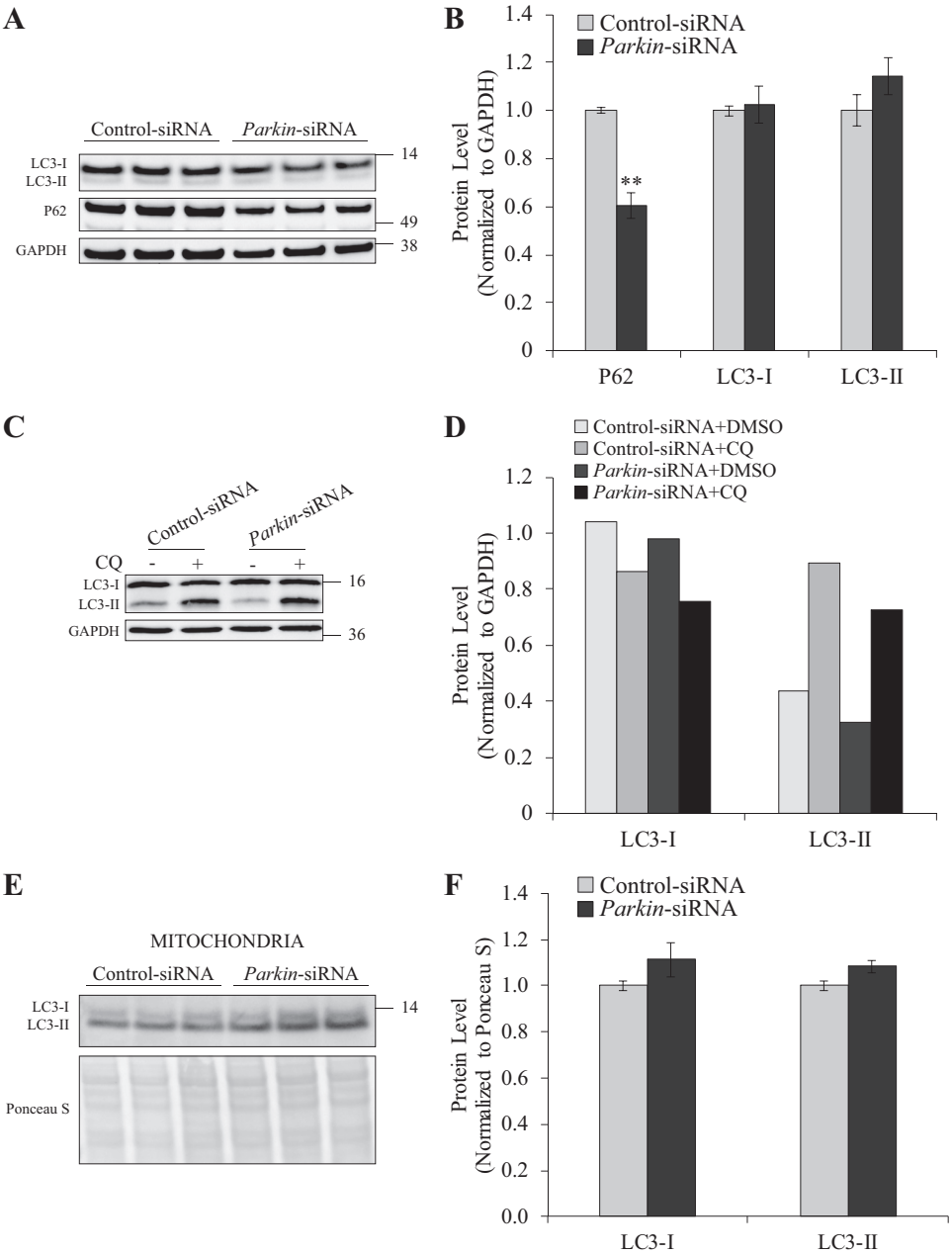

Fig. 5. Knockdown of *Parkin* does not alter autophagy in vitro. *A*: representative images of Western blot analysis of nonlipidated LC3 (LC3-I), lipidated LC-3 (LC3-II), and p62 protein levels in Control-siRNA and *Parkin*-siRNA-transfected myoblasts. The levels of GAPDH were assessed as a loading control. *B*: graph showing quantification of p62, LC3-I, and LC3-II, normalized to GAPDH, in arbitrary units ($n = 3$). *C*: representative images of Western blot analysis of LC3-I and LC3-II protein levels in Control-siRNA and *Parkin*-siRNA-transfected myoblasts treated with either chloroquine (+) or control (−) for 24 h. Each band represents results from 3 independent samples pooled together. The levels of GAPDH were assessed as a loading control. *D*: graph showing the levels of LC3-I and LC3-II, normalized to GAPDH, in arbitrary units. *E*: representative Western blot images of LC3-I and LC3-II in mitochondrial fraction collected from Control-siRNA and *Parkin*-siRNA-transfected myotubes. Ponceau S represents equal loading ($n = 3$). *F*: graph showing the levels of LC3-I and LC3-II as normalized to Ponceau S, in arbitrary units ($n = 3$). With the exception of the graph in *D*, all graphs display means ± SE. $^{**}P < 0.01$ (Student's *t*-test).

Downloaded from journals.physiology.org/journal/ajpcell (065.021.193.086) on February 24, 2022.

knockdown myoblasts, as measured through assessment of fluorescent H_2DCFDA (Fig. 6*G*). In addition, FACS analysis revealed a significant increase in the levels of mitochondrial superoxide in *Parkin* knockdown myoblasts, when compared with controls (Fig. 6*H*), as assessed through quantifying the levels of MitoSOX red. Moreover, increased levels of active phosphorylated AMPKα were also observed in *Parkin* knockdown myoblasts, when compared with controls (Fig. 6, *I* and

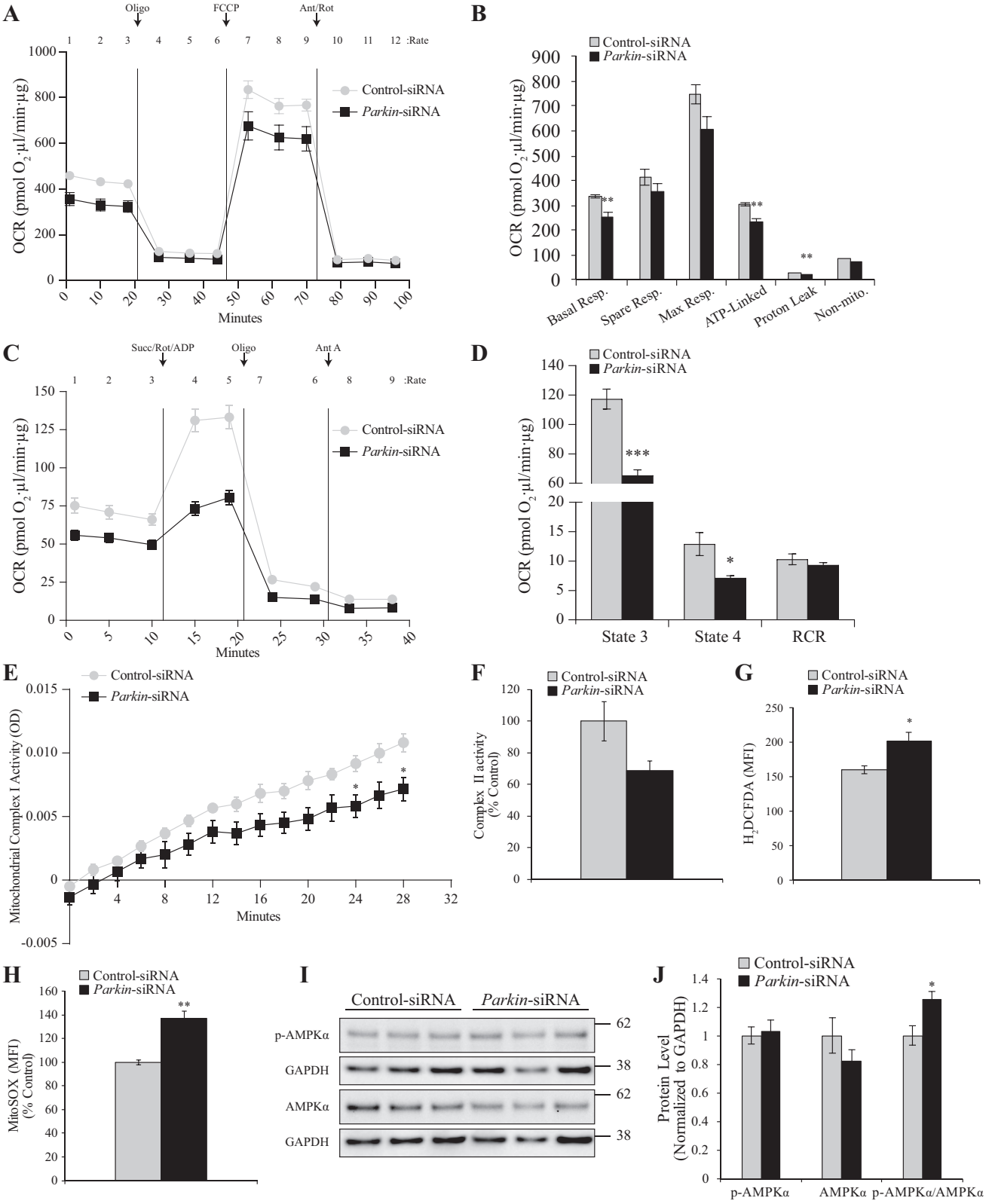

Downloaded from journals.physiology.org/journal/ajpcell (065.021.193.086) on February 24, 2022.

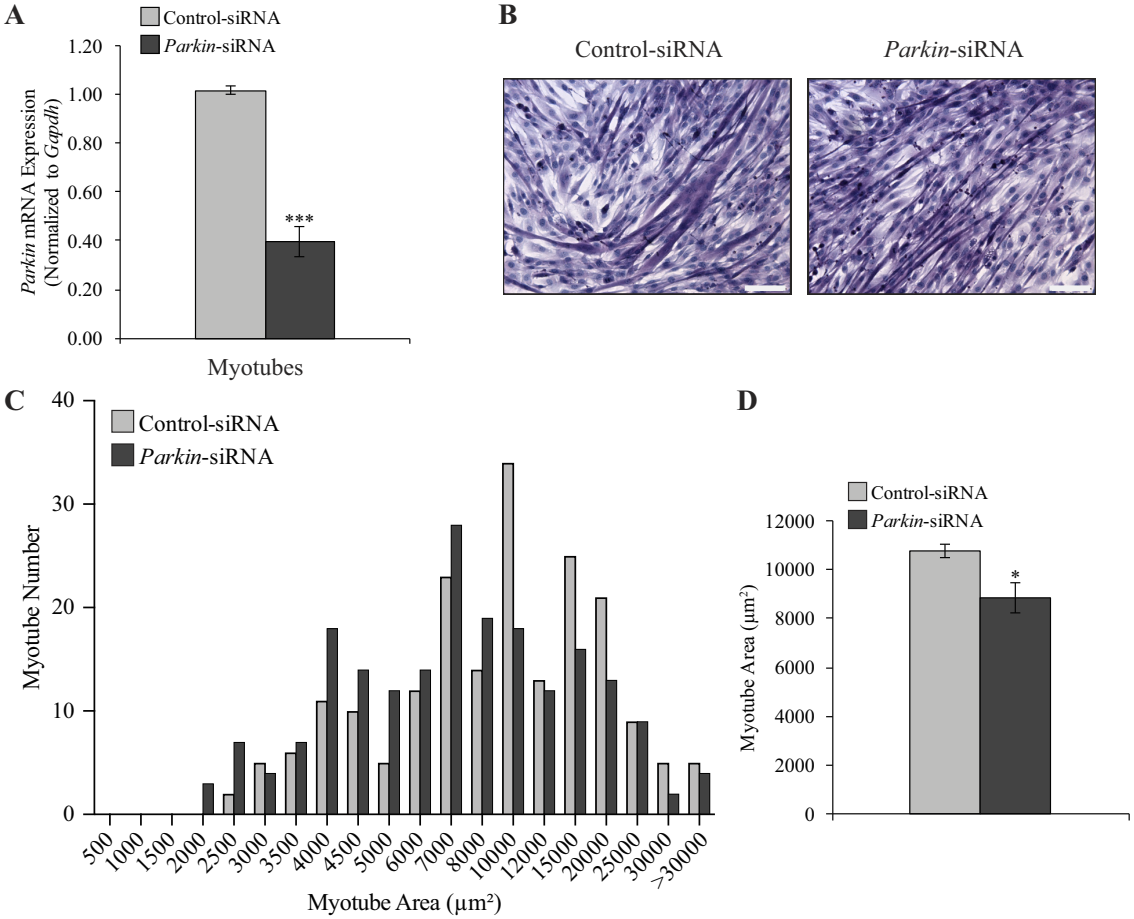

Fig. 7. *Parkin* knockdown myotubes exhibit a myotube atrophy phenotype in vitro. *A*: graph showing qPCR analysis of *Parkin* mRNA expression, normalized to *Gapdh*, in 120 h differentiated Control-siRNA and *Parkin*-siRNA-transfected myotubes ($n = 3$). *B*: representative images of H&E-stained 120 h differentiated Control-siRNA and *Parkin*-siRNA-transfected myotube. Scale bars, 100 μm. *C*: graph showing the distribution of myotube area in 120 h differentiated Control-siRNA and *Parkin*-siRNA-transfected myotubes ($n = 4$). *D*: graph showing average myotube area in 120 h differentiated Control-siRNA and *Parkin*-siRNA transfected myotubes ($n = 4$). With exception of the frequency distribution graph (*C*), all graphs represent means ± SE. $*P < 0.05$ and $***P < 0.001$ (Student's *t*-test).

J), further supporting impaired mitochondrial function upon knockdown of *Parkin*. Collectively, these data reveal that *Parkin* knockdown in myoblasts prevents overt mitophagy and results in the accumulation of dysfunctional mitochondria in vitro.

Knockdown of Parkin results in myotubular atrophy in vitro. To ascertain the effect of knockdown of *Parkin* and subsequent accumulation of dysfunctional mitochondria on myotube phenotype, we next transfected C2C12 myotubes with either Control or *Parkin* siRNA. qPCR analysis of *Parkin* expression confirmed knockdown of *Parkin* in C2C12 myotube cultures (Fig. 7*A*). Subsequent histological analysis of H&E-stained myotubes revealed notable myotubular atrophy in *Parkin* knockdown myotubes (Fig. 7*B*). Subsequent quantification

Fig. 6. *Parkin* knockdown results in reduced mitochondrial respiration, decreased mitochondrial complex I activity, and elevated reactive oxygen species levels in vitro. *A*: graph showing the real-time oxygen consumption rate (OCR) of Control-siRNA and *Parkin*-siRNA-transfected myoblasts, as assessed by the Seahorse XF^{e}24 extracellular flux analyzer ($n = 5$). Time points where oligomycin (Oligo), FCCP, and antimycin/rotenone (Ant/Rot) were injected (arrows) and the rate number where each OCR was measured are indicated. *B*: graph showing quantification of basal, spare, maximal, ATP-linked and nonmitochondrial respiration, and respiration due to proton leak in Control-siRNA and *Parkin*-siRNA-transfected myoblasts. All OCR values were normalized to total protein ($n = 5$). *C*: graph showing the real-time OCR of permeabilized Control-siRNA and *Parkin*-siRNA-transfected myoblasts ($n = 10$). Time points where succinate+rotenone+ADP (Succ/Rot/ADP), oligomycin (Oligo), and antimycin A (Ant A) were injected (arrows) and the rate number where each OCR was measured are indicated. *D*: graph showing quantification of State 3, State 4, and respiratory control ratio (RCR) in permeabilized Control-siRNA and *Parkin*-siRNA-transfected myoblasts. All OCR values were normalized to total protein ($n = 10$). *E*: graph representing mitochondrial complex I activity in mitochondrial fraction isolated from Control-siRNA and *Parkin*-siRNA-transfected myotubes ($n = 3$). *F*: graph showing activity of mitochondrial complex II in mitochondrial fractions collected from *Parkin*-siRNA-transfected myotubes and control ($n = 3$). *G*: graph showing the levels of reactive oxygen species, as measured by H_2DCFDA fluorescence, in Control-siRNA and *Parkin*-siRNA-transfected myoblasts ($n = 4$). MFI, mean fluorescence intensity. *H*: graph showing the levels of mitochondrial superoxide, as assessed through MitoSOX fluorescence, in Control-siRNA and *Parkin*-siRNA-transfected myoblasts ($n = 3$). *I*: representative images of Western blot analysis of phosphorylated AMPKα (p-AMPKα) and total AMPKα protein levels in Control-siRNA and *Parkin*-siRNA-transfected myoblasts. The levels of GAPDH were assessed as a loading control for each respective blot ($n = 3$). *J*: graph showing quantification of p-AMPKα, total AMPKα, and ratio of p-AMPKα/total AMPKα, normalized to GAPDH, in arbitrary units ($n = 3$). All graphs display means ± SE. $*P < 0.05$, $**P < 0.01$, $***P < 0.001$ (Student's *t*-test).

Downloaded from journals.physiology.org/journal/ajpcell (065.021.193.086) on February 24, 2022.

revealed a shift in myotube area distribution, with increased small (<10,000 μm^2) and decreased large (>10,000 μm^2) myotubes noted (Fig. 7*C*) In addition, a significant ~18% reduction in average myotube area was also observed in *Parkin* knockdown myotubes, when compared with controls (Fig. 7*D*). These data reveal that knockdown of *Parkin* in myoblasts not only results in accumulation of defective mitochondria, but also leads to myotubular atrophy.

Mitochondrial function is impaired in Parkin KO mice, despite maintenance of mitochondrial number. Given that knockdown of *Parkin* in vitro results in impaired mitochondrial function, we next assessed for changes in mitochondrial content and function in skeletal muscle and primary myoblast cultures derived from *Parkin* KO mice. Although a trend towards increased mitochondrial DNA (mtDNA) copy number was noted in *Parkin* KO primary myoblast cultures (Fig. 8*A*),

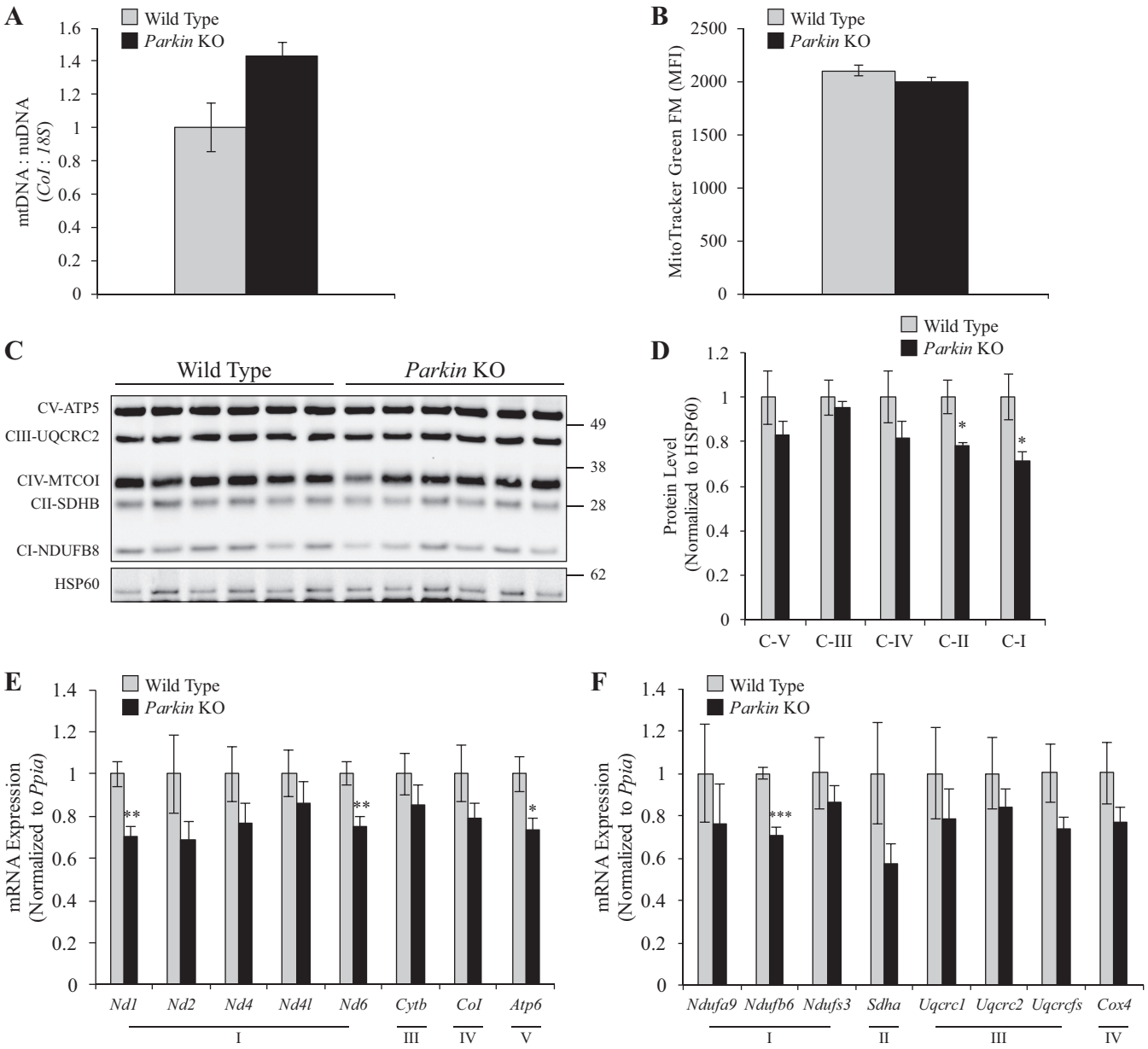

Fig. 8. Loss of *Parkin* results in reduced OXPHOS protein levels, while preserving the mitochondrial pool. *A*: graph showing qPCR analysis of mtDNA copy number (mtDNA):nuDNA copy number (nuDNA) ratio in primary myotubes isolated from wild-type and *Parkin* knockout (KO) mice. Values are expressed as fold change relative to wild-type control. The expression of the mitochondrial gene *CoI* was normalized to the nuclear gene *18S* ($n = 3$). *B*: graph showing results of FACS analysis of MitoTracker Green FM-stained primary myoblasts isolated from wild-type or *Parkin* KO mice ($n = 3$). MFI, mean fluorescence intensity. *C*: representative images of Western blot analysis of OXPHOS subunit (ATP5, UQCRC2, MTCOI, SDHB, and NDUFB8) protein levels in wild-type and *Parkin* KO gastrocnemius (Gas) muscle. The levels of heat shock protein 60 (HSP60) were assessed as a loading control ($n = 6$). *D*: graph showing quantification of OXPHOS protein levels, normalized to HSP60, in arbitrary units ($n = 6$). *E*: graph showing qPCR analysis of mitochondria DNA-encoded mitochondrial complex gene expression, normalized to *Ppia*, in wild-type and *Parkin* KO Gas muscle ($n = 6$). *F*: graph showing qPCR analysis of nuclear DNA-encoded mitochondrial complex gene expression, normalized to *Ppia*, in wild-type and *Parkin* KO Gas muscle ($n = 6$). All graphs show means ± SE. $*P < 0.05$, $**P < 0.01$, $***P < 0.001$ (Student's t-test).

Downloaded from journals.physiology.org/journal/ajpcell (065.021.193.086) on February 24, 2022.

the increase was not statistically significant. Similarly, no significant difference in mitochondrial content, as assessed through MitoTracker Green FM staining and FACS analysis, was noted in *Parkin* KO primary myoblast cultures (Fig. 8*B*). Despite no significant difference in mitochondrial number, a trend towards reduced levels of mitochondrial OXPHOS proteins (Complex I–V) was revealed in Gas muscle isolated from *Parkin* KO mice, when compared with wild-type controls (Fig.

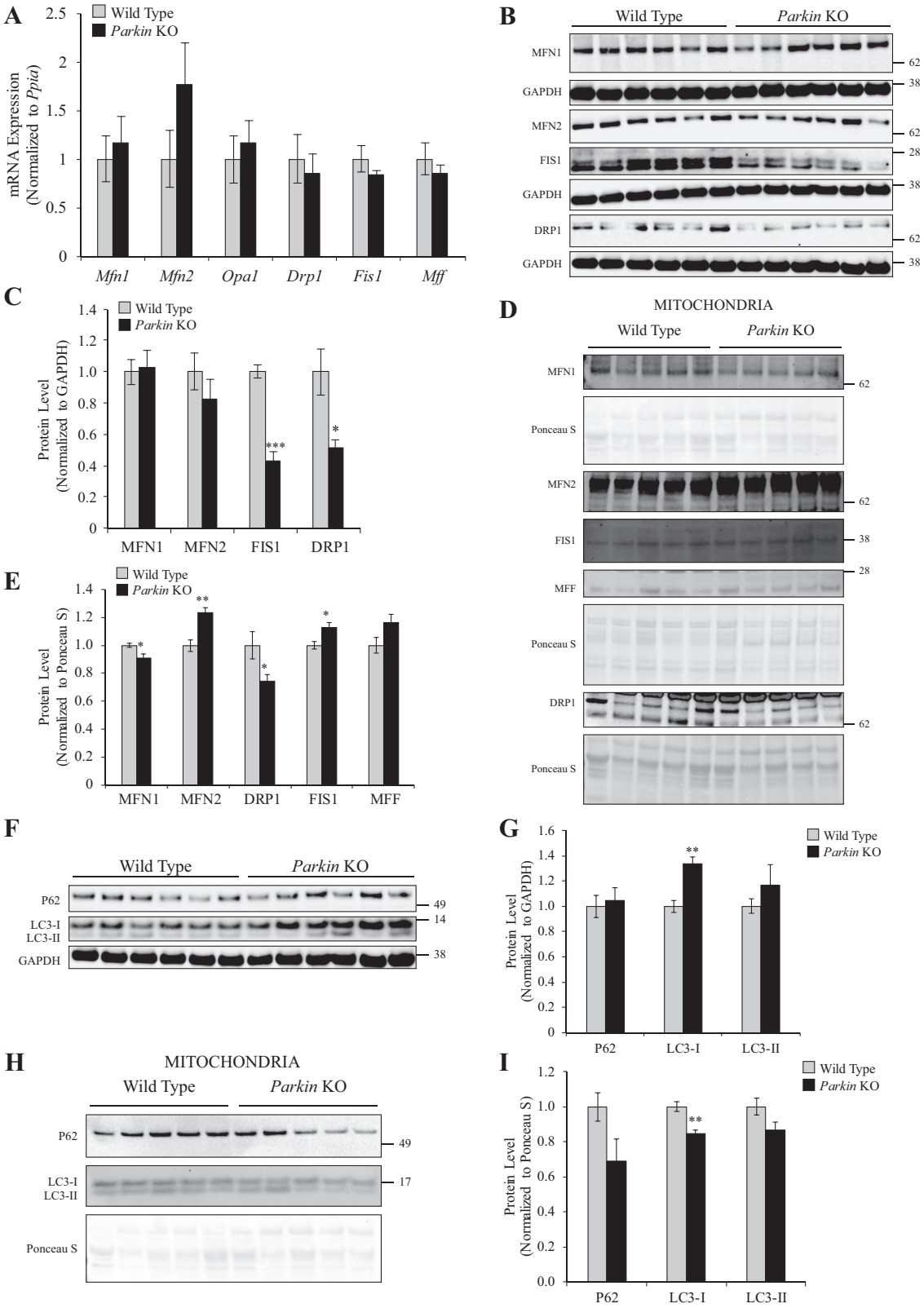

Downloaded from journals.physiology.org/journal/ajpcell (065.021.193.086) on February 24, 2022.

8, *C* and *D*). Notably, a significant reduction in the levels of the Complex I protein NDUFB8 and the Complex II protein SDHB were observed (Fig. 8, *C* and *D*). Consistent with this, decreased expression of both mitochondrial-encoded (Fig. 8*E*) and nuclear-encoded (Fig. 8*F*) mitochondrial complex genes was also observed in Gas muscle isolated from *Parkin* KO mice, with a significant reduction in *Nd1*, *Nd6*, *Atp6*, and *Ndufb6* expression noted (Fig. 8, *E* and *F*).

We next performed qPCR to quantify the expression of genes critical for mitochondrial fusion (*Mfn1*, *Mfn2*, and *Opa1*) and mitochondrial fission (*Drp1*, *Fis1*, and *Mff*) in skeletal muscle isolated from wild-type and *Parkin* KO mice. As shown in Fig. 9*A*, no significant difference in the mRNA expression of mitochondrial fusion and fission markers was observed in Gas muscle isolated from wild-type and *Parkin* KO mice (Fig. 9*A*). Subsequent immunoblot analysis revealed no significant difference in the levels of both MFN1 and MFN2 mitochondrial fusion proteins (Fig. 9, *B* and *C*), which is in agreement with the qPCR results. However, a significant reduction in the protein levels of the mitochondrial fission markers FIS1 and DRP1 was noted in *Parkin* KO Gas muscle tissue, when compared with wild-type controls (Fig. 9, *B* and *C*). Moreover, we assessed the levels of mitochondrial turnover marker proteins in mitochondrial fractions collected from *Parkin* KO Gas muscle tissue. Western blot analysis revealed a slight but significant increase in the levels of MFN2 and FIS1 proteins, together with a significant, albeit modest, reduction in the levels of MFN1 and DRP1 proteins (Fig. 9, *D* and *E*). Despite subtle, but significant, differences in the levels of non-lipidated LC3-I, the levels of the autophagosomal markers lipidated LC3-II and p62 were not significantly altered in either total muscle tissue (Fig. 9, *F* and *G*) or mitochondrial fractions (Fig. 9, *H* and *I*) isolated from wild-type and *Parkin* KO mice, suggesting that loss of *Parkin* does not result in overt autophagy/mitophagy in skeletal muscle. Taken together, these data reveal that mitochondria number is preserved in *Parkin* KO mice and that loss of *Parkin* leads to changes in gene expression consistent with decreased mitochondrial respiration and impaired mitochondrial turnover in skeletal muscle.

Next, we measured mitochondrial function in primary myotube cultures derived from wild-type and *Parkin* KO mice through real-time assessment of OCR using the Seahorse XF^{e}24 extracellular flux analyzer. An overall reduction in real-time oxygen consumption rate was apparent in *Parkin* KO myotubes (Fig. 10*A*). Moreover, a significant reduction in basal, maximum, ATP-linked, and nonmitochondrial respiration was noted in *Parkin* KO myotubes (Fig. 10, *A* and *B*). In addition, a significant reduction in spare respiratory capacity and OCR due to proton leak was further observed in *Parkin* KO myotubes, when compared with wild-type controls (Fig. 10*B*). Consistent with impaired mitochondrial function, we observed a dramatic reduction in activity of mitochondrial Complex I and Complex II (Fig. 10, *C* and *D*). Moreover, increased levels of ROS (Fig. 10*E*) and active p-AMPK protein (Fig. 10, *F* and *G*) were detected in primary myoblasts harvested from *Parkin* KO mice, when compared with wild-type controls, although the increase in p-AMPK was not statistically significant (Fig. 10*G*). Taken together, these data suggest that, whereas mitochondrial number remains unchanged, mitochondrial function is impaired in skeletal muscle of *Parkin* KO mice.

Absence of Parkin results in reduced body weight, decreased skeletal muscle weight, and myofiber atrophy in mice. As knockdown of *Parkin* in myotubes resulted in myotubular atrophy, we next assessed the phenotype of *Parkin* KO mice. *Parkin* KO mice have significantly reduced total body weight at 4 wk of age, when compared with age-matched wild-type mice controls (Fig. 11*A*). To confirm absence of *Parkin* in skeletal muscle tissues collected from *Parkin* KO mice, we performed immunoblot analysis; no detectable levels of PARKIN protein were observed in M. quadriceps (Quad), M. gastrocnemius (Gas), M. tibialis anterior (TA), M. soleus (Sol), and M. extensor digitorum longus (EDL) hindlimb muscles (Fig. 11*B*). Further characterization of hindlimb skeletal muscle tissue weights revealed a significant reduction in the weights of all hindlimb muscles analyzed in *Parkin* KO mice, when compared with wild-type controls (Fig. 11, *C* and *D*). Consistent with this, subsequent histological analysis (Fig. 11*E*) of myofiber cross-sectional area (CSA) in OCT embedded H&E stained TA muscles, revealed a reduction in TA myofiber CSA distribution (Fig. 11*F*), average myofiber CSA (Fig. 11*G*), and entire TA muscle CSA (Fig. 11*H*) in *Parkin* KO mice, when compared with wild-type controls, which is indicative of skeletal muscle atrophy in *Parkin* KO mice. These data suggest that loss of *Parkin* results in reduced skeletal muscle mass in vivo.

DISCUSSION

CCCP induces PINK1/PARKIN-mediated mitophagy in C2C12 myotubes. Mutations in *PARKIN* have been shown to be a primary susceptibility factor for development of familial PD (3). Identification of *PARKIN* as a critical factor involved in mitochondrial quality control resulted in further studies to investigate mitochondrial function in PD. Over the past two decades, research on PD has revealed that mutations in the

Fig. 9. *Parkin* knockout (KO) mice have impaired mitochondrial turnover but do not have overt mitophagy and autophagy. *A*: graph showing qPCR analysis of mRNA expression of mitochondrial fusion (*Mfn1*, *Mfn2*, *Opa1*) and fission (*Drp1*, *Fis1*, *Mff*) markers in wild-type and *Parkin* KO gastrocnemius (Gas) muscle ($n = 6$). *B*: representative images of Western blot analysis of mitofusin-1 (MFN1), mitofusin-2 (MFN2), FIS1 and dynamin-related protein 1 (DRP1) in wild-type and *Parkin* KO Gas muscle. The levels of GAPDH were assessed as a loading control ($n = 6$). *C*: graph showing quantification of MFN1, MFN2, FIS1, and DRP1 protein levels, normalized to GAPDH, in arbitrary units ($n = 6$). *D*: representative images of Western blot analysis of MFN1, MFN2, FIS1, mitochondrial fission factor (MFF), and DRP1 in mitochondrial fractions isolated from wild type-and *Parkin* KO Gas muscle. The levels of Ponceau S were assessed as a loading control ($n = 5$). *E*: graph showing quantification of MFN1, MFN2, DRP1, FIS1, and MFF protein levels, normalized to Ponceau S, in arbitrary units ($n = 5$). *F*: representative images of Western blot analysis of p62, LC3-I, and LC3-II protein levels in wild-type and *Parkin* KO Gas muscle. The levels of GAPDH were assessed as a loading control ($n = 6$). *G*: graph showing quantification of p62, LC3-I, and LC3-II protein levels, normalized to GAPDH, in arbitrary units ($n = 6$). *H*: representative Western blot images of p62, LC3-I, and LC3-II protein levels in mitochondrial fractions isolated from wild-type and *Parkin* KO Gas muscle. Ponceau S is represented to show equal loading ($n = 5$). *I*: graph showing quantification of p62, LC3-I, and LC3-II, normalized to Ponceau S, in arbitrary units ($n = 5$). Graphs show means ± SE. $^*P < 0.05$, $^{**}P < 0.01$, $^{***}P < 0.001$ (Student's *t*-test).

Downloaded from journals.physiology.org/journal/ajpcell (065.021.193.086) on February 24, 2022.

PARKIN gene lead to impaired mitochondrial function, turnover, and morphology (23, 37, 53). Although it is known that *PARKIN*-mediated alterations of mitochondrial homeostasis contribute to the onset of PD, little is presently known about PARKIN function in skeletal muscle or for that matter what changes occur to skeletal muscle post-natal development in response to altered PARKIN levels. To this end we have undertaken studies to provide insight into the emerging role of PARKIN in regulation of skeletal muscle function using both in vitro and in vivo models.

CCCP is a mitochondrial uncoupler that is commonly used in mitophagy research. Previous work has documented that CCCP leads to reduced mitochondrial membrane potential, thereby resulting in mitochondrial swelling in vitro (38, 44).

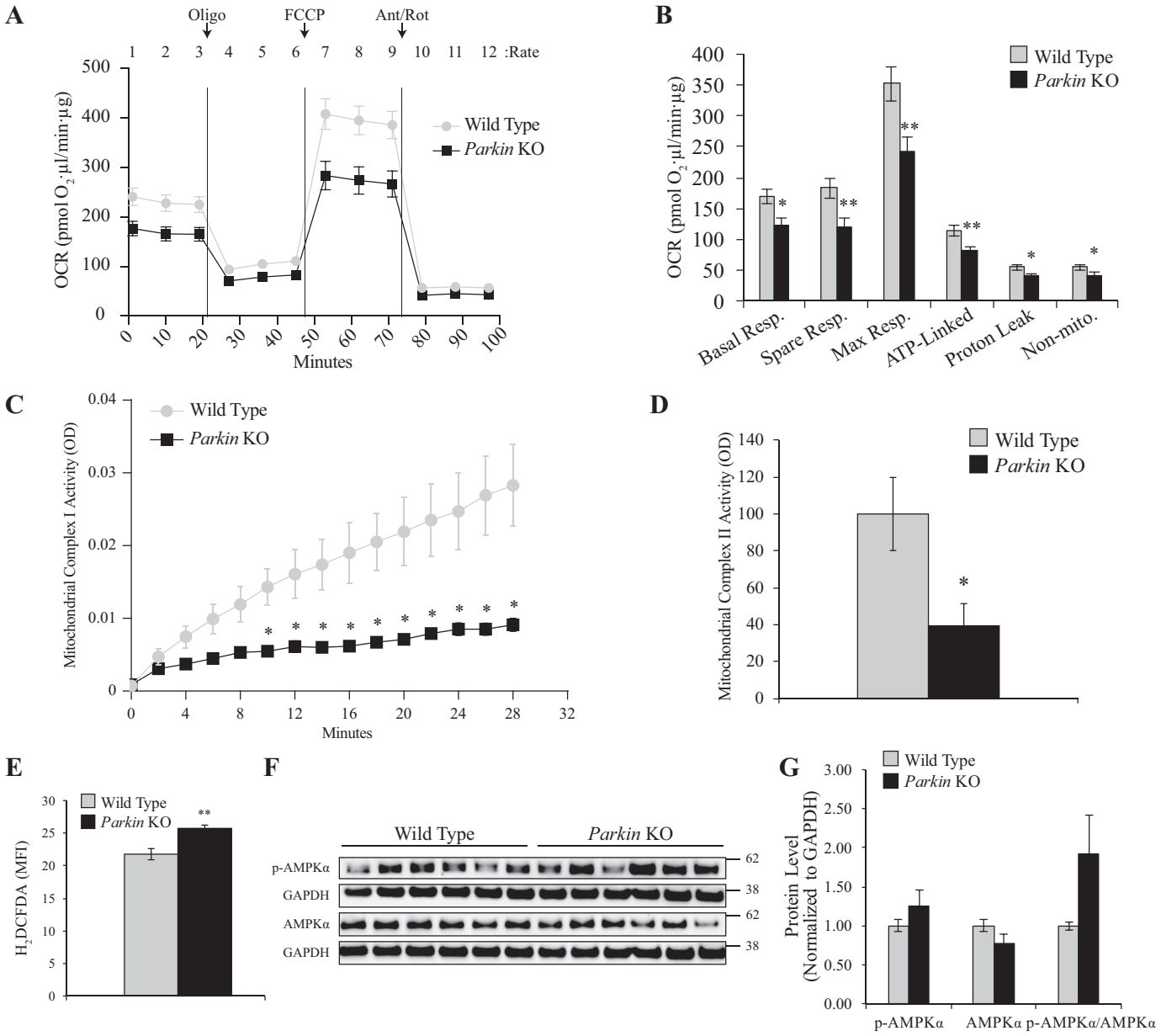

Fig. 10. *Parkin* knockout (KO) mice display reduced mitochondrial respiration, complex I and complex II activity and elevated reactive oxygen species (ROS) levels. A: graph showing the real-time oxygen consumption rate (OCR) measurement of 72 h differentiated primary myotubes isolated from wild-type and *Parkin* KO hindlimb muscles, as assessed by the Seahorse XF^{e}24 extracellular flux analyzer (n = 9). Time points where oligomycin (Oligo), FCCP and antimycin/rotenone (Ant/Rot) were injected (arrows) and the rate number where each OCR was measured are indicated. *B*: graph showing quantification of basal, spare, maximal, ATP-linked and nonmitochondrial respiration, and respiration due to proton leak in 72 h differentiated primary myotubes isolated from wild-type and *Parkin* KO hindlimb muscles. All OCR values were normalized to total protein (n = 9). *C*: graph representing mitochondrial complex I activity in mitochondrial fraction isolated from wild-type and *Parkin* KO gastrocnemius (Gas) muscle (n = 5). *D*: graph showing activity of mitochondrial complex II in mitochondrial fractions collected from wild-type and *Parkin* KO Gas muscle (n = 5). *E*: graph showing the levels of ROS, as measured by H_2DCFDA fluorescence, in 72 h differentiated primary myotubes isolated from wild type-and *Parkin* KO hindlimb muscles (n = 4). *F*: representative images of Western blot analysis of phosphorylated (p-AMPKα) and total AMPKα protein levels in wild-type and *Parkin* KO Gas muscle. The levels of GAPDH were assessed as a loading control (n = 6). *G*: graph showing quantification of p-AMPKα, total AMPKα, and the ratio of p-AMPKα/total AMPKα, normalized to GAPDH, in arbitrary units (n = 6). All graphs show means ± SE. $^*P < 0.05$, $^{**}P < 0.01$ (Student's t-test).

Downloaded from journals.physiology.org/journal/ajpcell (065.021.193.086) on February 24, 2022.

Although the fact that addition of CCCP leads to PINK1/PARKIN-mediated mitophagy in HeLa (49), HEK-293, and HCT-116 (61) cells, the effect of CCCP on mitochondrial function and turnover in skeletal muscle and, moreover, the effect of CCCP treatment on skeletal muscle mass have not been extensively studied. In line with previous reports, we have shown that treatment of C2C12 myotubes with CCCP results in pronounced mitophagy through activation of the

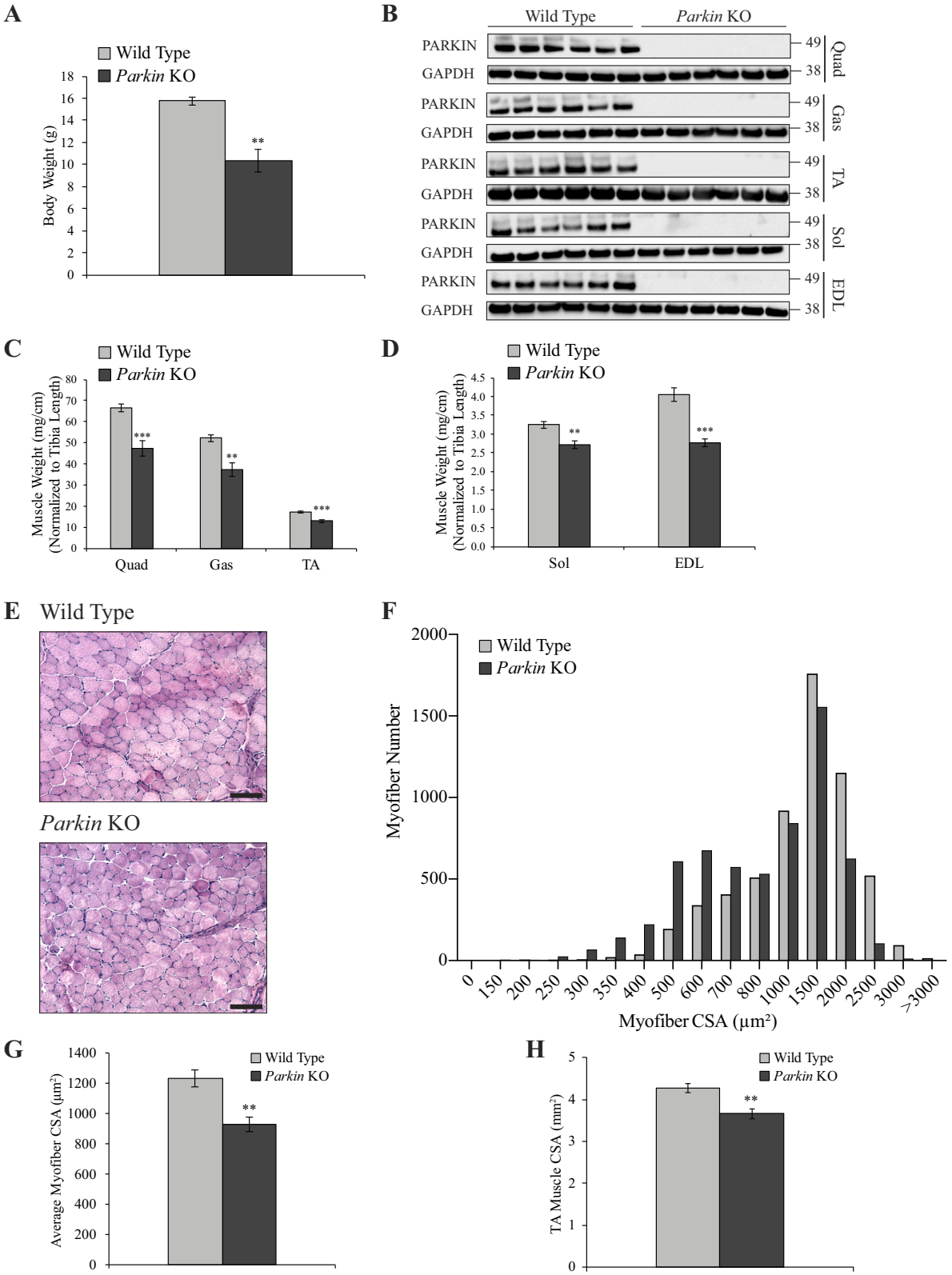

Downloaded from journals.physiology.org/journal/ajpcell (065.021.193.086) on February 24, 2022.

PINK1/PARKIN pathway. Specifically, we found that CCCP treatment leads to increased levels of active full-length PINK1 protein (63 kDa) (Fig. 1*B*); These data suggest that in response to CCCP treatment, PINK1 protein is somewhat protected from processing through the action of mitochondrial processing peptidase and the presilin-associated rhomboid-like protease, which promote the formation of a 53-kDa cleaved PINK1 protein (21). In response to increased levels of full-length PINK1 protein we also noted enhanced recruitment of PARKIN to mitochondria (Fig. 1*C*). Mitochondrial reticulum targeted by PARKIN exhibits reduced mitochondrial mass and respiratory capacity. Consistent with this, CCCP treatment resulted in loss of mitochondria number and reduced mitochondrial function, as determined through decreased cellular respiration, activation of the energy sensor AMPK, and increased ER stress. Previous studies have reported that mitochondrial dysfunction contributes to disuse atrophy and dexamethasone-driven atrophy in skeletal muscle (27, 39, 54). Consistent with this, histological analysis of myotubes treated with CCCP revealed pronounced myotubular atrophy in vitro. These data suggest that disruption of energy homeostasis in skeletal muscle tissue, through interference with mitochondria function and turnover, results in loss of skeletal muscle mass. It has been suggested by Romanello et al. (58), that loss of mitochondria and impaired mitochondrial function results in a negative energy balance in skeletal muscle, which drives loss of muscle mass.

Loss of Parkin results in mitochondrial dysfunction in skeletal muscle. PARKIN maintains the quality of mitochondrial reticulum by not only promoting the fission/fragmentation of damaged mitochondria, but also by inhibiting the fusion of damaged mitochondria through promoting the degradation of mitochondrial fusion proteins (16, 20). This function of PARKIN was further confirmed in recent studies, which showed that overexpression of *Parkin* improves mitochondrial function and protects from proteotoxicity, suggesting that selective elimination of damaged mitochondria enhances cellular homeostasis (56, 72). Consistent with these findings, we observed that knockdown of *Parkin* resulted in increased mitochondrial mass but decreased mitochondrial function. On the basis of our results, we propose that loss of PARKIN results in impaired mitochondrial turnover and accumulation of dysfunctional mitochondria.

In line with previous observations that have reported reduced mitochondrial complex activity in parkinsonism phenotype (8, 34, 51, 55), we observed a tendency towards reduced levels of mitochondrial complex proteins in the absence of *Parkin*, with a significant reduction in Complex I (NDUFB8) and Complex II (SDHB) subunits noted in *Parkin* KO skeletal muscle. More importantly, loss of *Parkin* also resulted in reduced mitochondrial Complex I and Complex II activity both in vitro and in vivo, providing further support that loss of *Parkin* leads to mitochondrial dysfunction in skeletal muscle. However, it is important to highlight that we observed a significant increase in the mRNA expression of several nuclear-DNA-encoded mitochondrial OXPHOS genes (Fig. 4*G*). Previous studies have documented increased mRNA expression of OXPHOS genes in diseases associated with mitochondrial complex deficiencies (57). Therefore, we speculate that the increased mRNA expression of OXPHOS genes observed in *Parkin* knockdown cells may act to compensate for the reduced OXPHOS protein levels and impaired mitochondrial function noted.

Mitochondria have a critical function in lowering the levels of cellular ROS (24). Consistent with impaired mitochondrial function, we noted elevated levels of ROS in both *Parkin* knockdown myoblasts and in *Parkin* knockout primary myoblasts (Fig. 6, *G* and *H* and Fig. 10*E*). A recent study has revealed that knockdown of the mitochondrial Complex I assembly factor NDUFAF1 results in decreased OXPHOS and increased ROS production (45), which is similar to the phenotype we noted in the current study. Therefore, the reduced levels of mitochondrial complex proteins noted in the absence of *Parkin* may result in the elevated ROS and mitochondrial dysfunction observed.

AMPK is the well-studied energy sensor of the cell. Under stress conditions, elevated AMP:ATP and ADP:ATP ratios trigger activation of AMPK, which results in increased catabolism and reduced anabolism (66). In PD, a negative role has been proposed for AMPK. Two independent studies have reported that inhibition of AMPK has a neuroprotective role in PD (78), while activation of AMPK results in atrophy of dopaminergic neurons (30, 78). Data presented here (using both in vitro and in vivo models) show that loss of *Parkin* leads to increased levels of active phosphorylated AMPKα. We speculate that mitochondrial dysfunction in skeletal muscle due to loss of *Parkin* results in energy deprivation, subsequent activation of AMPK, and increased catabolism, which is consistent with the previously described function of AMPK in maintaining energy homeostasis (25).

Nevertheless; these data collectively suggest that loss of *Parkin* has a detrimental effect on mitochondrial turnover and mitochondrial function in skeletal muscle, which further underscores the importance of *Parkin* function to skeletal muscle metabolism.

Loss of Parkin leads to skeletal muscle atrophy in vitro and in vivo. Individuals with PD display symptoms such as muscle weakness, resistance to exercise, and fatigue (33). Similarly, knockout of *parkin* in *Drosophila* leads to defective locomotion (22). Consistent with the impaired skeletal muscle func-

Fig. 11. Four-week-old *Parkin* knockout (KO) mice have reduced muscle weights and myofiber size. *A*: graph showing average body weights of 4-wk-old wild-type and *Parkin* KO mice ($n = 6$). *B*: representative images of Western blot images showing PARKIN protein levels in musculus (M) quadriceps (Quad), M. gastrocnemius (Gas), and M. tibialis anterior (TA), M. soleus (Sol), and M. extensor digitorum longus (EDL) muscles of wild-type and *Parkin* KO mice. The levels of GAPDH were assessed as a loading control ($n = 6$). *C*: graph showing weights of M. quadriceps (Quad), M. gastrocnemius (Gas), and M. tibialis anterior (TA) muscles of wild-type and *Parkin* KO mice. All hindlimb muscle weights were normalized to tibia length ($n = 6$). *D*: graph showing weights of M. soleus (Sol) and M. extensor digitorum longus (EDL) muscles of wild-type and *Parkin* KO mice. All hindlimb muscle weights were normalized to tibia length ($n = 6$). *E*: representative images of hematoxylin and eosin (H&E)-stained M. tibialis anterior (TA) muscle sections of 4-wk-old wild-type and *Parkin* KO mice. Scale bars, 100 μm. *F*: graph showing the distribution of myofiber cross-sectional area (CSA) in 4-wk-old wild-type and *Parkin* KO mice TA muscles ($n = 6$). *G*: graph showing average myofiber CSA of 4-wk-old wild-type and *Parkin* KO mice TA muscles ($n = 6$). *H*: graph showing CSA of entire TA muscle sections obtained from 4-wk-old wild-type and *Parkin* KO mice ($n = 6$). All graphs show means ± SE. $^{**}P < 0.01$ and $^{***}P < 0.001$ (Student's *t*-test).

Downloaded from journals.physiology.org/journal/ajpcell (065.021.193.086) on February 24, 2022.

tion described above, we found that loss of *Parkin* in myoblasts resulted in observable myotubular atrophy. As described above, knockdown, or complete loss of, *Parkin* leads to increased levels of active p-AMPKα. Recent work has revealed that AMPK is able to regulate the levels of FoxO transcription factors, which promote the expression of atrophy-related genes (atrogenes), such as MuRF1, resulting in skeletal muscle atrophy (32, 47). Therefore, it is interesting to surmise that loss of *Parkin* may result in skeletal muscle atrophy through upregulation of AMPK. In addition, increased ROS levels have been associated with induction of skeletal muscle wasting (9, 41, 42). Thus, it is plausible that increased levels of ROS, as observed in response to loss of *Parkin*, may also be involved in the muscle atrophy phenotype observed.

Conclusion. Here we have assessed the role of PARKIN in mitochondrial function in skeletal muscle. In this study, we provide evidence that perturbations in mitochondrial turnover and function (due to inactivation of PARKIN) lead to muscular atrophy. Furthermore, we reveal that loss of *Parkin* leads to mitochondrial dysfunction, elevated ROS levels and impaired mitochondrial turnover both in vitro and in vivo. Consistent with impaired mitochondrial function, we find activation of the energy sensor AMPK, which is in agreement with the loss of skeletal muscle mass observed in response to reduced *Parkin*. Future studies should be aimed at further defining the molecular mechanism(s) through which absence of *Parkin* leads to skeletal muscle wasting.

ACKNOWLEDGMENTS

We thank National University of Singapore (NUS) Confocal Microscopy Unit for help with confocal imaging in this manuscript. The monoclonal antibodies against MF-20 and T-14 developed by Weill Cornell Medical College and Stockdale, F. E., respectively, were obtained from the Developmental Studies Hybridoma Bank (DSHB), created by the National Institute of Child Health and Human Development of the NIH and maintained at The University of Iowa, Department of Biology, Iowa City, IA 52242.

M. Sharma and R. Kambadur are no longer affiliated with institutions listed. Present address of C. McFarlane: Dept. of Molecular and Cell Biology, College of Public Health, Medical and Veterinary Sciences, James Cook Univ., 1 James Cook Drive, Townsville, QLD 4811 Australia (e-mail: craig.mcfarlane@jcu.edu.au).

GRANTS

We are indebted to the Agency for Science, Technology and Research (A*STAR), Singapore for financial support. Nesibe Peker is a PhD student funded by the Turkish Education Foundation and Singapore International Graduate Student Award (TEV-SINGA).

DISCLOSURES

No conflicts of interest, financial or otherwise, are declared by the authors.

AUTHOR CONTRIBUTIONS

N.P., M.S., C.M., and R.K. conceived and designed research; N.P. and V.D. performed experiments; N.P., V.D., M.S., C.M., and R.K. analyzed data; N.P., V.D., M.S., C.M., and R.K. interpreted results of experiments; N.P. prepared figures; N.P., M.S., C.M., and R.K. drafted manuscript; N.P., V.D., M.S., C.M., and R.K. edited and revised manuscript; N.P., V.D., M.S., C.M., and R.K. approved final version of manuscript.

REFERENCES

1. **Attaix D, Ventadour S, Codran A, Béchet D, Taillandier D, Combaret L.** The ubiquitin-proteasome system and skeletal muscle wasting. *Essays Biochem* 41: 173–186, 2005. doi:10.1042/bse0410173.
2. **Blin O, Desnuelle C, Rascol O, Borg M, Peyro Saint Paul H, Azulay JP, Billé F, Figarella D, Coulom F, Pellissier JF, Montastruc JL, Chatel M, Serratrice G.** Mitochondrial respiratory failure in skeletal muscle from patients with Parkinson's disease and multiple system atrophy. *J Neurol Sci* 125: 95–101, 1994. doi:10.1016/0022-510X(94)90248-8.
3. **Bruggemann N, Klein C.** Parkin type of early-onset Parkinson disease. In: *GeneReviews*, edited by Pagon RA, Adam MP, Ardinger HH, Wallace SE, Amemiya A, Bean LJH, Bird TD, Ledbetter N, Mefford HC, Smith RJH, Stephens K. Seattle, WA, Univ. of Washington, 1993.
4. **Cao Z, Wanagat J, McKiernan SH, Aiken JM.** Mitochondrial DNA deletion mutations are concomitant with ragged red regions of individual, aged muscle fibers: analysis by laser-capture microdissection. *Nucleic Acids Res* 29: 4502–4508, 2001. doi:10.1093/nar/29.21.4502.
5. **Cardellach F, Martí MJ, Fernández-Solá J, Marín C, Hoek JB, Tolosa E, Urbano-Márquez A.** Mitochondrial respiratory chain activity in skeletal muscle from patients with Parkinson's disease. *Neurology* 43: 2258–2262, 1993. doi:10.1212/WNL.43.11.2258.
6. **Castillo-Quan JI.** Parkin' control: regulation of PGC-1α through PARIS in Parkinson's disease. *Dis Model Mech* 4: 427–429, 2011. doi:10.1242/dmm.008227.
7. **Dauer W, Przedborski S.** Parkinson's disease: mechanisms and models. *Neuron* 39: 889–909, 2003. doi:10.1016/S0896-6273(03)00568-3.
8. **Davis GC, Williams AC, Markey SP, Ebert MH, Caine ED, Reichert CM, Kopin IJ.** Chronic Parkinsonism secondary to intravenous injection of meperidine analogues. *Psychiatry Res* 1: 249–254, 1979. doi:10.1016/0165-1781(79)90006-4.
9. **Dodd SL, Gagnon BJ, Senf SM, Hain BA, Judge AR.** Ros-mediated activation of NF-kappaB and Foxo during muscle disuse. *Muscle Nerve* 41: 110–113, 2010. doi:10.1002/mus.21526.
10. **Drew BG, Ribas V, Le JA, Henstridge DC, Phun J, Zhou Z, Soleymani T, Daraei P, Sitz D, Vergnes L, Wanagat J, Reue K, Febbraio MA, Hevener AL.** HSP72 is a mitochondrial stress sensor critical for Parkin action, oxidative metabolism, and insulin sensitivity in skeletal muscle. *Diabetes* 63: 1488–1505, 2014. doi:10.2337/db13-0665.
11. **Falvo MJ, Schilling BK, Earhart GM.** Parkinson's disease and resistive exercise: rationale, review, and recommendations. *Mov Disord* 23: 1–11, 2008. doi:10.1002/mds.21690.
12. **Forno LS.** Neuropathology of Parkinson's disease. *J Neuropathol Exp Neurol* 55: 259–272, 1996. doi:10.1097/00005072-199603000-00001.
13. **Furuya N, Ikeda S, Sato S, Soma S, Ezaki J, Oliva Trejo JA, Takeda-Ezaki M, Fujimura T, Arikawa-Hirasawa E, Tada N, Komatsu M, Tanaka K, Kominami E, Hattori N, Ueno T.** PARK2/Parkin-mediated mitochondrial clearance contributes to proteasome activation during slow-twitch muscle atrophy via NFE2L1 nuclear translocation. *Autophagy* 10: 631–641, 2014. doi:10.4161/auto.27785.
14. **Garber CE, Friedman JH.** Effects of fatigue on physical activity and function in patients with Parkinson's disease. *Neurology* 60: 1119–1124, 2003. doi:10.1212/01.WNL.0000055868.06222.AB.
15. **García-Ruiz I, Solís-Muñoz P, Fernández-Moreira D, Muñoz-Yagüe T, Solís-Herruzo JA.** In vitro treatment of HepG2 cells with saturated fatty acids reproduces mitochondrial dysfunction found in nonalcoholic steatohepatitis. *Dis Model Mech* 8: 183–191, 2015. doi:10.1242/dmm.018234.
16. **Gegg ME, Schapira AH.** PINK1-parkin-dependent mitophagy involves ubiquitination of mitofusins 1 and 2: implications for Parkinson disease pathogenesis. *Autophagy* 7: 243–245, 2011. doi:10.4161/auto.7.2.14332.
17. **Geisler S, Holmström KM, Skujat D, Fiesel FC, Rothfuss OC, Kahle PJ, Springer W.** PINK1/Parkin-mediated mitophagy is dependent on VDAC1 and p62/SQSTM1. *Nat Cell Biol* 12: 119–131, 2010. doi:10.1038/ncb2012.
18. **Gershanik OS, Nygaard TG.** Parkinson's disease beginning before age 40. *Adv Neurol* 53: 251–258, 1990.
19. **Giasson BI, Lee VM.** Parkin and the molecular pathways of Parkinson's disease. *Neuron* 31: 885–888, 2001. doi:10.1016/S0896-6273(01)00439-1.
20. **Glauser L, Sonnay S, Stafa K, Moore DJ.** Parkin promotes the ubiquitination and degradation of the mitochondrial fusion factor mitofusin 1. *J Neurochem* 118: 636–645, 2011. doi:10.1111/j.1471-4159.2011.07318.x.
21. **Greene AW, Grenier K, Aguileta MA, Muise S, Farazifard R, Haque ME, McBride HM, Park DS, Fon EA.** Mitochondrial processing peptidase regulates PINK1 processing, import and Parkin recruitment. *EMBO Rep* 13: 378–385, 2012. doi:10.1038/embor.2012.14.
22. **Greene JC, Whitworth AJ, Kuo I, Andrews LA, Feany MB, Pallanck LJ.** Mitochondrial pathology and apoptotic muscle degeneration in *Dro-*

Downloaded from journals.physiology.org/journal/ajpcell (065.021.193.086) on February 24, 2022.

sophila parkin mutants. *Proc Natl Acad Sci USA* 100: 4078–4083, 2003. doi:10.1073/pnas.0737556100.
23. **Grünewald A, Voges L, Rakovic A, Kasten M, Vandebona H, Hemmelmann C, Lohmann K, Orolicki S, Ramirez A, Schapira AH, Pramstaller PP, Sue CM, Klein C.** Mutant Parkin impairs mitochondrial function and morphology in human fibroblasts. *PLoS One* 5: e12962, 2010. doi:10.1371/journal.pone.0012962.
24. **Handy DE, Loscalzo J.** Redox regulation of mitochondrial function. *Antioxid Redox Signal* 16: 1323–1367, 2012. doi:10.1089/ars.2011.4123.
25. **Hardie DG, Ross FA, Hawley SA.** AMPK: a nutrient and energy sensor that maintains energy homeostasis. *Nat Rev Mol Cell Biol* 13: 251–262, 2012. doi:10.1038/nrm3311.
26. **Jagoe RT, Goldberg AL.** What do we really know about the ubiquitin-proteasome pathway in muscle atrophy? *Curr Opin Clin Nutr Metab Care* 4: 183–190, 2001. doi:10.1097/00075197-200105000-00003.
27. **Jheng HF, Tsai PJ, Guo SM, Kuo LH, Chang CS, Su IJ, Chang CR, Tsai YS.** Mitochondrial fission contributes to mitochondrial dysfunction and insulin resistance in skeletal muscle. *Mol Cell Biol* 32: 309–319, 2012. doi:10.1128/MCB.05603-11.
28. **Julienne CM, Dumas JF, Goupille C, Pinault M, Berri C, Collin A, Tesseraud S, Couet C, Servais S.** Cancer cachexia is associated with a decrease in skeletal muscle mitochondrial oxidative capacities without alteration of ATP production efficiency. *J Cachexia Sarcopenia Muscle* 3: 265–275, 2012. doi:10.1007/s13539-012-0071-9.
29. **Kane LA, Lazarou M, Fogel AI, Li Y, Yamano K, Sarraf SA, Banerjee S, Youle RJ.** PINK1 phosphorylates ubiquitin to activate Parkin E3 ubiquitin ligase activity. *J Cell Biol* 205: 143–153, 2014. doi:10.1083/jcb.201402104.
30. **Kim TW, Cho HM, Choi SY, Suguira Y, Hayasaka T, Setou M, Koh HC, Hwang EM, Park JY, Kang SJ, Kim HS, Kim H, Sun W.** (ADP-ribose) polymerase 1 and AMP-activated protein kinase mediate progressive dopaminergic neuronal degeneration in a mouse model of Parkinson's disease. *Cell Death Dis* 4: e919, 2013. doi:10.1038/cddis.2013.447.
31. **Koyano F, Okatsu K, Kosako H, Tamura Y, Go E, Kimura M, Kimura Y, Tsuchiya H, Yoshihara H, Hirokawa T, Endo T, Fon EA, Trempe JF, Saeki Y, Tanaka K, Matsuda N.** Ubiquitin is phosphorylated by PINK1 to activate parkin. *Nature* 510: 162–166, 2014. doi:10.1038/nature13392.
32. **Krawiec BJ, Nystrom GJ, Frost RA, Jefferson LS, Lang CH.** AMP-activated protein kinase agonists increase mRNA content of the muscle-specific ubiquitin ligases MAFbx and MuRF1 in C2C12 cells. *Am J Physiol Endocrinol Metab* 292: E1555–E1567, 2007. doi:10.1152/ajpendo.00622.2006.
33. **Lang AE, Lozano AM.** Parkinson's disease. First of two parts. *N Engl J Med* 339: 1044–1053, 1998. doi:10.1056/NEJM199810083391506.
34. **Langston JW, Ballard P, Tetrud JW, Irwin I.** Chronic Parkinsonism in humans due to a product of meperidine-analog synthesis. *Science* 219: 979–980, 1983. doi:10.1126/science.6823561.
35. **Leal SS, Gomes CM.** Calcium dysregulation links ALS defective proteins and motor neuron selective vulnerability. *Front Cell Neurosci* 9: 225, 2015. doi:10.3389/fncel.2015.00225.
36. **Lee CM, Lopez ME, Weindruch R, Aiken JM.** Association of age-related mitochondrial abnormalities with skeletal muscle fiber atrophy. *Free Radic Biol Med* 25: 964–972, 1998. doi:10.1016/S0891-5849(98)00185-3.
37. **Lee JY, Nagano Y, Taylor JP, Lim KL, Yao TP.** Disease-causing mutations in parkin impair mitochondrial ubiquitination, aggregation, and HDAC6-dependent mitophagy. *J Cell Biol* 189: 671–679, 2010. doi:10.1083/jcb.201001039.
38. **Lim ML, Minamikawa T, Nagley P.** The protonophore CCCP induces mitochondrial permeability transition without cytochrome *c* release in human osteosarcoma cells. *FEBS Lett* 503: 69–74, 2001. doi:10.1016/S0014-5793(01)02693-X.
39. **Liu J, Peng Y, Wang X, Fan Y, Qin C, Shi L, Tang Y, Cao K, Li H, Long J, Liu J.** Mitochondrial dysfunction launches dexamethasone-induced skeletal muscle atrophy via AMPK/FOXO3 signaling. *Mol Pharm* 13: 73–84, 2016. doi:10.1021/acs.molpharmaceut.5b00516.
40. **Lücking CB, Dürr A, Bonifati V, Vaughan J, De Michele G, Gasser T, Harhangi BS, Meco G, Denèfle P, Wood NW, Agid Y, Nicholl D, Breteler MMB, Oostra BA, De Mari M, Marconi R, Filla A, Bonnet A-M, Broussolle E, Pollak P, Rascol O, Rosier M, Arnould A, Brice A; French Parkinson's Disease Genetics Study Group; European Consortium on Genetic Susceptibility in Parkinson's Disease.** Association between early-onset Parkinson's disease and mutations in the parkin gene. *N Engl J Med* 342: 1560–1567, 2000. doi:10.1056/NEJM200005253422103.
41. **McClung JM, Judge AR, Powers SK, Yan Z.** p38 MAPK links oxidative stress to autophagy-related gene expression in cachectic muscle wasting. *Am J Physiol Cell Physiol* 298: C542–C549, 2010. doi:10.1152/ajpcell.00192.2009.
42. **McClung JM, Judge AR, Talbert EE, Powers SK.** Calpain-1 is required for hydrogen peroxide-induced myotube atrophy. *Am J Physiol Cell Physiol* 296: C363–C371, 2009. doi:10.1152/ajpcell.00497.2008.
43. **McFarlane C, Hennebry A, Thomas M, Plummer E, Ling N, Sharma M, Kambadur R.** Myostatin signals through Pax7 to regulate satellite cell self-renewal. *Exp Cell Res* 314: 317–329, 2008. doi:10.1016/j.yexcr.2007.09.012.
44. **Minamikawa T, Williams DA, Bowser DN, Nagley P.** Mitochondrial permeability transition and swelling can occur reversibly without inducing cell death in intact human cells. *Exp Cell Res* 246: 26–37, 1999. doi:10.1006/excr.1998.4290.
45. **Miwa S, Jow H, Baty K, Johnson A, Czapiewski R, Saretzki G, Treumann A, von Zglinicki T.** Low abundance of the matrix arm of complex I in mitochondria predicts longevity in mice. *Nat Commun* 5: 3837, 2014. doi:10.1038/ncomms4837.
46. **Mu L, Sobotka S, Chen J, Su H, Sanders I, Adler CH, Shill HA, Caviness JN, Samanta JE, Beach TG; Arizona Parkinson's Disease Consortium.** Altered pharyngeal muscles in Parkinson disease. *J Neuropathol Exp Neurol* 71: 520–530, 2012. doi:10.1097/NEN.0b013e318258381b.
47. **Nakashima K, Yakabe Y.** AMPK activation stimulates myofibrillar protein degradation and expression of atrophy-related ubiquitin ligases by increasing FOXO transcription factors in C2C12 myotubes. *Biosci Biotechnol Biochem* 71: 1650–1656, 2007. doi:10.1271/bbb.70057.
48. **Narendra D, Tanaka A, Suen DF, Youle RJ.** Parkin-induced mitophagy in the pathogenesis of Parkinson disease. *Autophagy* 5: 706–708, 2009. doi:10.4161/auto.5.5.8505.
49. **Narendra D, Tanaka A, Suen DF, Youle RJ.** Parkin is recruited selectively to impaired mitochondria and promotes their autophagy. *J Cell Biol* 183: 795–803, 2008. doi:10.1083/jcb.200809125.
50. **Narendra D, Walker JE, Youle R.** Mitochondrial quality control mediated by PINK1 and Parkin: links to parkinsonism. *Cold Spring Harb Perspect Biol* 4: a011338, 2012. doi:10.1101/cshperspect.a011338.
51. **Nicklas WJ, Vyas I, Heikkila RE.** Inhibition of NADH-linked oxidation in brain mitochondria by 1-methyl-4-phenyl-pyridine, a metabolite of the neurotoxin, 1-methyl-4-phenyl-1,2,5,6-tetrahydropyridine. *Life Sci* 36: 2503–2508, 1985. doi:10.1016/0024-3205(85)90146-8.
52. **Ordureau A, Heo JM, Duda DM, Paulo JA, Olszewski JL, Yanishevski D, Rinehart J, Schulman BA, Harper JW.** Defining roles of PARKIN and ubiquitin phosphorylation by PINK1 in mitochondrial quality control using a ubiquitin replacement strategy. *Proc Natl Acad Sci USA* 112: 6637–6642, 2015. doi:10.1073/pnas.1506593112.
53. **Pacelli C, De Rasmo D, Signorile A, Grattagliano I, di Tullio G, D'Orazio A, Nico B, Comi GP, Ronchi D, Ferranini E, Pirolo D, Seibel P, Schubert S, Gaballo A, Villani G, Cocco T.** Mitochondrial defect and PGC-1α dysfunction in parkin-associated familial Parkinson's disease. *Biochim Biophys Acta* 1812: 1041–1053, 2011. doi:10.1016/j.bbadis.2010.12.022.
54. **Powers SK, Wiggs MP, Duarte JA, Zergeroglu AM, Demirel HA.** Mitochondrial signaling contributes to disuse muscle atrophy. *Am J Physiol Endocrinol Metab* 303: E31–E39, 2012. doi:10.1152/ajpendo.00609.2011.
55. **Ramsay RR, Salach JI, Dadgar J, Singer TP.** Inhibition of mitochondrial NADH dehydrogenase by pyridine derivatives and its possible relation to experimental and idiopathic parkinsonism. *Biochem Biophys Res Commun* 135: 269–275, 1986. doi:10.1016/0006-291X(86)90972-1.
56. **Rana A, Rera M, Walker DW.** Parkin overexpression during aging reduces proteotoxicity, alters mitochondrial dynamics, and extends lifespan. *Proc Natl Acad Sci USA* 110: 8638–8643, 2013. doi:10.1073/pnas.1216197110.
57. **Reinecke F, Smeitink JA, van der Westhuizen FH.** OXPHOS gene expression and control in mitochondrial disorders. *Biochim Biophys Acta* 1792: 1113–1121, 2009. doi:10.1016/j.bbadis.2009.04.003.
58. **Romanello V, Guadagnin E, Gomes L, Roder I, Sandri C, Petersen Y, Milan G, Masiero E, Del Piccolo P, Foretz M, Scorrano L, Rudolf R, Sandri M.** Mitochondrial fission and remodelling contributes to muscle atrophy. *EMBO J* 29: 1774–1785, 2010. doi:10.1038/emboj.2010.60.

Downloaded from journals.physiology.org/journal/ajpcell (065.021.193.086) on February 24, 2022.

59. **Romanello V, Sandri M.** Mitochondrial Quality Control and Muscle Mass Maintenance. *Front Physiol* 6: 422, 2016. doi:10.3389/fphys.2015.00422.
60. **Rosen KM, Veereshwarayya V, Moussa CE, Fu Q, Goldberg MS, Schlossmacher MG, Shen J, Querfurth HW.** Parkin protects against mitochondrial toxins and beta-amyloid accumulation in skeletal muscle cells. *J Biol Chem* 281: 12809–12816, 2006. doi:10.1074/jbc.M512649200.
61. **Sargsyan A, Cai J, Fandino LB, Labasky ME, Forostyan T, Colosimo LK, Thompson SJ, Graham TE.** Rapid parallel measurements of macroautophagy and mitophagy in mammalian cells using a single fluorescent biosensor. *Sci Rep* 5: 12397, 2015. doi:10.1038/srep12397.
62. **Shiba-Fukushima K, Imai Y, Yoshida S, Ishihama Y, Kanao T, Sato S, Hattori N.** PINK1-mediated phosphorylation of the Parkin ubiquitin-like domain primes mitochondrial translocation of Parkin and regulates mitophagy. *Sci Rep* 2: 1002, 2012. doi:10.1038/srep01002.
63. **Shin JH, Ko HS, Kang H, Lee Y, Lee YI, Pletinkova O, Troconso JC, Dawson VL, Dawson TM.** PARIS (ZNF746) repression of PGC-1α contributes to neurodegeneration in Parkinson's disease. *Cell* 144: 689–702, 2011. doi:10.1016/j.cell.2011.02.010.
64. **Shirwany NA, Zou MH.** AMPK: a cellular metabolic and redox sensor. A minireview. *Front Biosci (Landmark Ed)* 19: 447–474, 2014. doi:10.2741/4218.
65. **Song M, Mihara K, Chen Y, Scorrano L, Dorn GW II.** Mitochondrial fission and fusion factors reciprocally orchestrate mitophagic culling in mouse hearts and cultured fibroblasts. *Cell Metab* 21: 273–286, 2015. doi:10.1016/j.cmet.2014.12.011.
66. **Steinberg GR, Kemp BE.** AMPK in health and disease. *Physiol Rev* 89: 1025–1078, 2009. doi:10.1152/physrev.00011.2008.
67. **Stevens-Lapsley J, Kluger BM, Schenkman M.** Quadriceps muscle weakness, activation deficits, and fatigue with Parkinson disease. *Neurorehabil Neural Repair* 26: 533–541, 2012. doi:10.1177/1545968311425925.
68. **Tamura Y, Kitaoka Y, Matsunaga Y, Hoshino D, Hatta H.** Daily heat stress treatment rescues denervation-activated mitochondrial clearance and atrophy in skeletal muscle. *J Physiol* 593: 2707–2720, 2015. doi:10.1113/JP270093.
69. **Tanaka A, Cleland MM, Xu S, Narendra DP, Suen DF, Karbowski M, Youle RJ.** Proteasome and p97 mediate mitophagy and degradation of mitofusins induced by Parkin. *J Cell Biol* 191: 1367–1380, 2010. doi:10.1083/jcb.201007013.
70. **Thomas B Beal MF.** Parkinson's disease. *Hum Mol Genet* 16: R183–R194, 2007. doi:10.1093/hmg/ddm159.
71. **Twig G, Elorza A, Molina AJ, Mohamed H, Wikstrom JD, Walzer G, Stiles L, Haigh SE, Katz S, Las G, Alroy J, Wu M, Py BF, Yuan J, Deeney JT, Corkey BE, Shirihai OS.** Fission and selective fusion govern mitochondrial segregation and elimination by autophagy. *EMBO J* 27: 433–446, 2008. doi:10.1038/sj.emboj.7601963.
72. **Ulusoy A, Kirik D.** Can overexpression of parkin provide a novel strategy for neuroprotection in Parkinson's disease? *Exp Neurol* 212: 258–260, 2008. doi:10.1016/j.expneurol.2008.04.026.
73. **Wang D, Green MF, McDonnell E, Hirschey MD.** Oxygen flux analysis to understand the biological function of sirtuins. *Methods Mol Biol* 1077: 241–258, 2013. doi:10.1007/978-1-62703-637-5_16.
75. **Winkler-Stuck K, Kirches E, Mawrin C, Dietzmann K, Lins H, Wallesch CW, Kunz WS, Wiedemann FR.** Re-evaluation of the dysfunction of mitochondrial respiratory chain in skeletal muscle of patients with Parkinson's disease. *J Neural Transm (Vienna)* 112: 499–518, 2005. doi:10.1007/s00702-004-0195-y.
76. **Winklhofer KF, Haass C.** Mitochondrial dysfunction in Parkinson's disease. *Biochim Biophys Acta* 1802: 29–44, 2010. doi:10.1016/j.bbadis.2009.08.013.
77. **Wu JJ, Roth RJ, Anderson EJ, Hong EG, Lee MK, Choi CS, Neufer PD, Shulman GI, Kim JK, Bennett AM.** Mice lacking MAP kinase phosphatase-1 have enhanced MAP kinase activity and resistance to diet-induced obesity. *Cell Metab* 4: 61–73, 2006. doi:10.1016/j.cmet.2006.05.010.
78. **Xu Y, Liu C, Chen S, Ye Y, Guo M, Ren Q, Liu L, Zhang H, Xu C, Zhou Q, Huang S, Chen L.** Activation of AMPK and inactivation of Akt result in suppression of mTOR-mediated S6K1 and 4E-BP1 pathways leading to neuronal cell death in in vitro models of Parkinson's disease. *Cell Signal* 26: 1680–1689, 2014. doi:10.1016/j.cellsig.2014.04.009.
79. **Yaffe D, Saxel O.** Serial passaging and differentiation of myogenic cells isolated from dystrophic mouse muscle. *Nature* 270: 725–727, 1977. doi:10.1038/270725a0.
80. **Yang JY, Yang WY.** Bit-by-bit autophagic removal of parkin-labelled mitochondria. *Nat Commun* 4: 2428, 2013. doi:10.1038/ncomms3428.
81. **Yun J, Puri R, Yang H, Lizzio MA, Wu C, Sheng ZH, Guo M.** MUL1 acts in parallel to the PINK1/parkin pathway in regulating mitofusin and compensates for loss of PINK1/parkin. *eLife* 3: e01958, 2014. doi:10.7554/eLife.01958.

Downloaded from journals.physiology.org/journal/ajpcell (065.021.193.086) on February 24, 2022.